

## Hunting for Planetary Nebulae toward the Galactic Center

JIHYE HONG,<sup>1</sup> JANET P. SIMPSON,<sup>2</sup> DEOKKEUN AN,<sup>1</sup> ANGELA S. COTERA,<sup>2</sup> AND SOLANGE V. RAMÍREZ<sup>3</sup>

<sup>1</sup>*Department of Science Education, Ewha Womans University, 52 Ewhayeodae-gil, Seodaemun-gu, Seoul 03760, Korea; deokkeun@ewha.ac.kr*

<sup>2</sup>*SETI Institute, 189 Bernardo Avenue, Mountain View, CA 94043, USA*

<sup>3</sup>*Carnegie observatory, 813 Santa Barbara Street, Pasadena, CA 91101, USA*

Submitted to AJ

### ABSTRACT

We present near-infrared (IR) spectra of two planetary nebula (PN) candidates in close lines of sight toward the Galactic center (GC) using GNIRS at Gemini North. High-resolution images from radio continuum and narrow-band IR observations reveal ring-like morphologies of these objects, and their mid-IR spectra from the *Spitzer* Space Telescope exhibit rich emission lines from highly excited species such as [S IV], [Ne III], [Ne V], and [O IV]. We also derive elemental abundances using the Cloudy synthetic models, and find an excess amount of the *s*-process element Krypton in both targets, which supports their nature as PNe. We estimate foreground extinction toward each object using near-IR hydrogen recombination lines, and find significant visual extinctions ( $A_V > 20$ ). The distances inferred from the size versus surface brightness relation of other PNe are  $9.0 \pm 1.6$  kpc and  $7.6 \pm 1.6$  kpc for SSTGC 580183 and SSTGC 588220, respectively. These observed properties along with abundance patterns and their close proximity to Sgr A\* (projected distances  $\lesssim 20$  pc) make it highly probable that these objects are the first confirmed PNe objects in the nuclear stellar disk. The apparent scarcity of such objects resembles the extremely low rate of PN formation in old stellar systems, but is in line with the current rate of the sustained star formation activity in the Central Molecular Zone.

*Keywords:* Planetary nebulae(1249), Milky Way Galaxy(1054), Interstellar Line Emission (844), Galactic center (565)

### 1. INTRODUCTION

Most stars with initial masses less than  $\sim 8 M_\odot$  evolve into planetary nebulae (PNe) at the end of their lifetimes (see Balick & Frank 2002, and references therein), as long as their progenitor masses are large enough (see Jacoby et al. 1997). In our Galaxy, a large number of PNe ( $\sim 3,500$ ) have been discovered so far, many of which are associated with the Galactic bulge or thin disk (e.g., Parker et al. 2006; Miszalski et al. 2008; Jacoby et al. 2010; Sabin et al. 2014), serving as bright tracers for the kinematics (e.g., Durand et al. 1998; Beaulieu et al. 2000) and chemical abundance studies in the Milky Way (e.g., Stanghellini & Haywood 2018). However, it has been known for a while that this number

is an order of magnitude lower than expected from population synthesis models (e.g., Moe & De Marco 2006), and the majority of PN populations in the Milky Way remain to be discovered. The heavy dust obscuration near the Galactic plane is likely the main cause of such discrepancy (e.g., Jacoby & Steene 2004; Miszalski et al. 2008; Parker et al. 2012).

In this context, the absence of PNe in the nuclear bulge of the Milky Way (Serabyn & Morris 1996; Launhardt et al. 2002) can be understood to be the result of the large amount of foreground dust towards the Galactic center (GC;  $A_V \sim 30$ ), which essentially prohibits detections and identifications of PNe through the conventional method of measuring optical emission lines. The mass of the nuclear bulge is  $\sim 1.4 \times 10^9 M_\odot$  (Launhardt et al. 2002), which is approximately 10 times less massive than the kpc-scale classical bulge. The stellar populations in the nuclear bulge are

predominantly old (e.g., [Nogueras-Lara et al. 2020](#)), but may have distinct chemical properties from the classical bulge (e.g., [Schultheis et al. 2020](#)). Most of these stars are confined to the nuclear stellar disk, a rotating disk of stars around Sgr A\*. The nuclear stellar disk spatially overlaps with the Central Molecular Zone (CMZ; see [Morris & Serabyn 1996](#), and references therein), a massive reservoir of molecular gas clouds with a diameter of  $\sim 500$  pc and a total cloud mass of  $\sim 3\text{--}8 \times 10^7 M_\odot$  ([Dahmen et al. 1998](#); [Tsuboi et al. 1999](#)). Sustained star formation activities are observed throughout the region (e.g., [An et al. 2011](#); [Longmore et al. 2013](#)). Given that both the Galactic bulge and thin disk harbor a noticeable number of PNe, the lack of PNe in the nuclear bulge poses a challenge to our understanding of PN formation, stellar populations and evolution in the inner-most region of the Milky Way.

Recently, we have identified two objects, SSTGC 580183 (G359.963-0.120 or G-0.037-0.120) and SSTGC 588220 (G0.098-0.051), as candidate PNe ([Simpson 2018](#)) while analyzing mid-IR spectra of compact IR sources toward the CMZ ([An et al. 2009, 2011](#)). They show high excitation lines such as [Na III]  $7.3 \mu\text{m}$ , [Ne V]  $14.3 \mu\text{m}$  and  $24.3 \mu\text{m}$ , and [O IV]  $25.9 \mu\text{m}$ . These lines are not observed in typical H II regions, but are often seen in PNe with an extremely hot ( $3 \times 10^4 \lesssim T_{\text{eff}} \lesssim 2 \times 10^5$  K) central object (e.g., [Osterbrock & Ferland 2006](#); [Peimbert et al. 2017](#)). The two objects have also been observed in high-resolution radio observations and with near-IR narrow-band filters, revealing a ring-like nebulosity ([Wang et al. 2010](#); [Zhao et al. 2020](#)).

In this paper, we report near-IR spectroscopic follow-up observations of these two objects using the Gemini Near-Infrared Spectrograph (GNIRS; [Elias et al. 2006a,b](#)) at the Frederick C. Gillett Gemini North Telescope. Owing to a paucity of PNe toward the GC, both objects are unique, providing an opportunity to explore stellar evolution and chemical characteristics of stellar populations in the inner region of the Galaxy. Their probable location in the CMZ is an interesting aspect of this study, since the massive reservoir of molecular gas in the CMZ is known to maintain the most active star forming activities in the Milky Way ( $\sim 0.1 M_\odot \text{ yr}^{-1}$ ; [An et al. 2011](#); [Longmore et al. 2013](#)); they can be used to study chemical and kinematical properties of stars that are distinct from those of the other Galactic components.

The primary goal of this study is to confirm the nature of these nebular sources as PNe and to characterize their chemical properties based on near-IR and mid-IR spectra. The near-IR spectra are particularly useful for this

purpose, because hydrogen recombination lines can be used to constrain foreground extinction, which is necessary to derive elemental abundances of ionic species from mid-IR spectra. This paper is organized as follows. In § 2, we describe observing tactics and data reduction. In § 3, we present GNIRS spectra, derive foreground extinction from hydrogen recombination lines, and put a constraint on their distances from a comparison with size versus surface brightness relations of PNe. We conduct a joint analysis of near-IR and mid-IR spectra in § 4 to derive elemental abundances. A summary of the work is provided in § 5.

## 2. OBSERVATIONS AND DATA REDUCTION

### 2.1. Candidates

Both SSTGC 580183 ( $\alpha = 17\text{h } 46\text{m } 0.034\text{s}$ ,  $\delta = -29^\circ 1' 50.210''$ ) and SSTGC 588220 ( $\alpha = 17\text{h } 46\text{m } 2.984\text{s}$ ,  $\delta = -28^\circ 52' 45.320''$ ) were originally identified as compact (within a  $2''$  beam) sources in the *Spitzer* Space Telescope ([Werner et al. 2004](#)) Infrared Array Camera (IRAC; [Fazio et al. 2004](#)) images ([Ramírez et al. 2008](#)). They were targeted for follow-up observation using the Infrared Spectrograph (IRS; [Houck et al. 2004](#)) onboard *Spitzer* ([An et al. 2009, 2011](#)), as part of a search for massive young stellar objects in the CMZ. There are no parallax measurements, but their proximity to the GC (with a projected angular distance of  $\sim 7'$ ) was deemed as a supporting piece of evidence for their potential membership in the CMZ, which covers a region of  $\sim 3^\circ \times 0.5^\circ$  centered at the GC.

Figure 1 shows mid-IR spectra of each target, taken using the high-resolution modules of IRS (see [An et al. 2009, 2011](#), for more details). The background emission from surrounding clouds in the CMZ was subtracted from the spectrum of each target using a set of background spectra (see below). The continuum of the background spectra is characterized by warm-dust emission and strong emission from polycyclic aromatic hydrocarbons at  $6.2$ ,  $7.7$ ,  $11.3$ ,  $12.7$ , and  $16.4 \mu\text{m}$ ; nonetheless, they are a factor of  $\sim 2\text{--}3$  times fainter than the target spectrum in the short-high (SH) module ( $10 \mu\text{m} \lesssim \lambda \lesssim 20 \mu\text{m}$ ), and  $\sim 5\text{--}8$  times fainter in the long-high (LH) module ( $20 \mu\text{m} \lesssim \lambda \lesssim 30 \mu\text{m}$ ). There are also a number of strong emission lines seen in the background spectra, which originate from diffuse ionized gas and photo-dissociation regions (PDRs) in molecular clouds adjacent to each target.

The mean background spectrum of the high-resolution modules was constructed using IRS observations at four carefully chosen locations ( $\sim 1'$  away in each direction) with the same instrument setup. Figure 2 shows emission lines observed in the IRS spectra after the back-

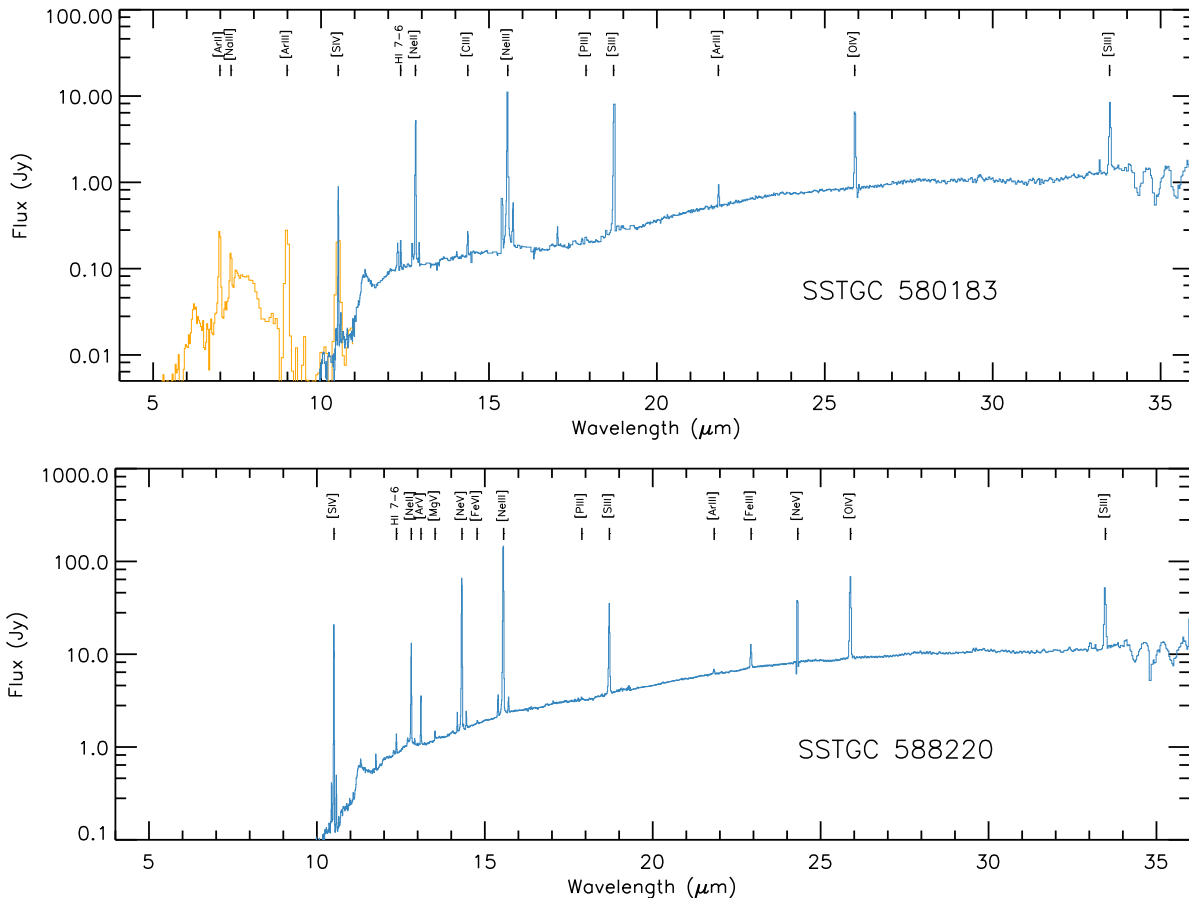


**Figure 1.** Background-subtracted *Spitzer*/IRS spectra of PN candidates. Spectra from high-resolution modules are shown by blue lines. For SSTGC 580183, low-resolution spectra are displayed by orange lines.

ground subtraction. Strong PDR emission lines from  $\text{H}_2$  S(2)  $12.28 \mu\text{m}$  and  $\text{H}_2$  S(1)  $17.04 \mu\text{m}$  are negligible after background subtraction. On the other hand, while some forbidden emission lines from highly excited ion species such as [S IV]  $10.51 \mu\text{m}$  and [O IV]  $25.89 \mu\text{m}$  are not visible or very weak in the background spectra, they are clearly seen in the background-subtracted spectra.<sup>1</sup> SSTGC 588220 additionally exhibits emission from [Ar V]  $13.10 \mu\text{m}$ , [Mg V]  $13.52 \mu\text{m}$ , and [Fe VI]  $14.77 \mu\text{m}$ . Such lines are commonly observed in PNe from gas ionized by a source of temperature  $\sim 10^5$  K, rather than from typical H II regions ionized by massive OB stars (e.g., Osterbrock & Ferland 2006).

## 2.2. Observations and Data Reduction

Medium-resolution ( $R \sim 2600$ ) near-IR ( $1.05 \mu\text{m}$  to  $2.22 \mu\text{m}$ ) spectra of the two PN candidates were taken using Gemini/GNIRS. A  $0.675'' \times 7''$  slit with the  $110.5$

$\text{mm}^{-1}$  grating was used in cross-dispersed (XD) mode with the short-blue camera ( $0.15''$  per pixel); the slit width was set to approximately match the seeing during the observation. Both targets were observed in queue observing runs; SSTGC 580183 was observed twice on March 11 and April 16 in 2016, respectively, with the former observation taken with a non-zero parallactic angle (see below). SSTGC 588220 was observed on March 19, 2016. The sky was mostly clear and the seeing was stable ( $0.5''$ – $0.7''$ ) during the observations.

Figure 3 displays locations of GNIRS slits for SSTGC 580183, overlaid on top of the UKIDSS (Lawrence et al. 2007) *K*-band image (top panel) and a Jansky Very Large Array (JVLA) 5.5 GHz radio image (Zhao et al. 2020, bottom). It was not resolved in earlier radio observations (Yusef-Zadeh et al. 2004; Mills et al. 2011), but the higher resolution image in Zhao et al. (2020) clearly reveals a ring-like structure with a diameter of  $\sim 4''$  along the major axis. The GNIRS slit was put nearly at the center of the ring.

As displayed in Figure 4, SSTGC 588220 was observed in the high-resolution ( $\sim 0.2''$ ), Paschen- $\alpha$  imaging

<sup>1</sup> [O IV]  $25.89 \mu\text{m}$  is saturated in the high-resolution IRS spectrum of SSTGC 588220, for which we used the low-resolution IRS spectrum in the modeling (see below).

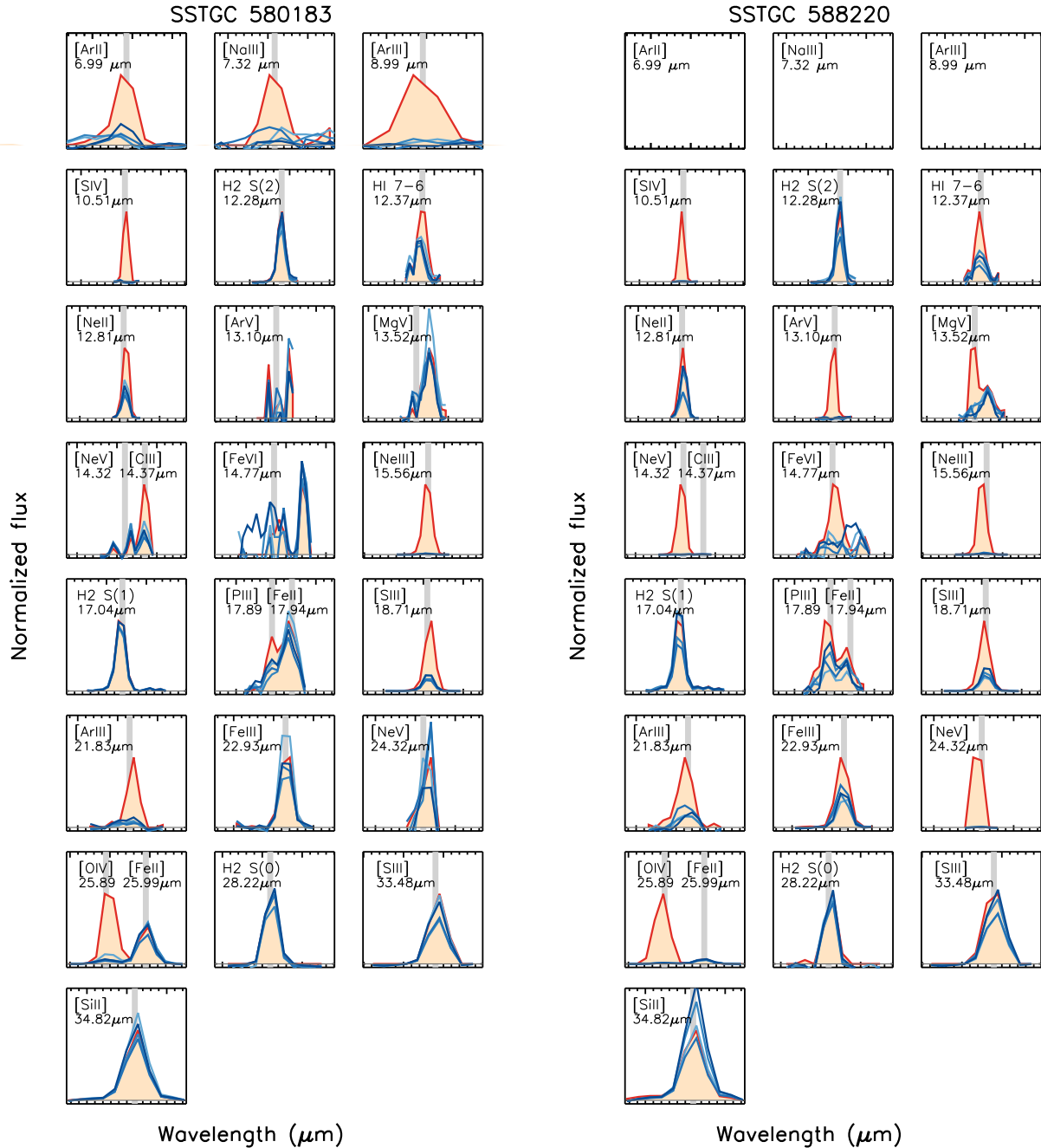


**Figure 2.** Emission lines in the *Spitzer*/IRS spectra of the PN candidates. Original line emissions from each target are shown by the orange-shaded red lines, while the blue lines show emission lines extracted at four nearby locations that do not contain bright point sources in the slit. Line centers are marked by a vertical grey stripe. Each panel spans a wavelength range of  $0.3 \mu\text{m}$  (each tick mark covers  $\Delta\lambda = 0.02 \mu\text{m}$ ).

survey using the *Hubble Space Telescope* (Wang et al. 2010). It reveals a bipolar structure of strong emission near the center, and a fainter, elongated ring-like structure, which is orthogonal to the axis of the inner lobes. The observed morphology is reminiscent of a quadrupolar PN (e.g., Manchado et al. 1996). The center of the slit for SSTGC 588220 was positioned on the brightest part of the nebula, which is the eastern lobe in the

*HST*/NICMOS image. The position angle at the time of observation was set to the parallactic angle; fortuitously, the slit included not only the eastern rim of the central region but also a part of the northern (fainter) ring.

Because of the high source density in the GC, the off-source slit position was carefully chosen near each target, and a background spectrum was obtained in an on-off sequence. A total on-source exposure time was

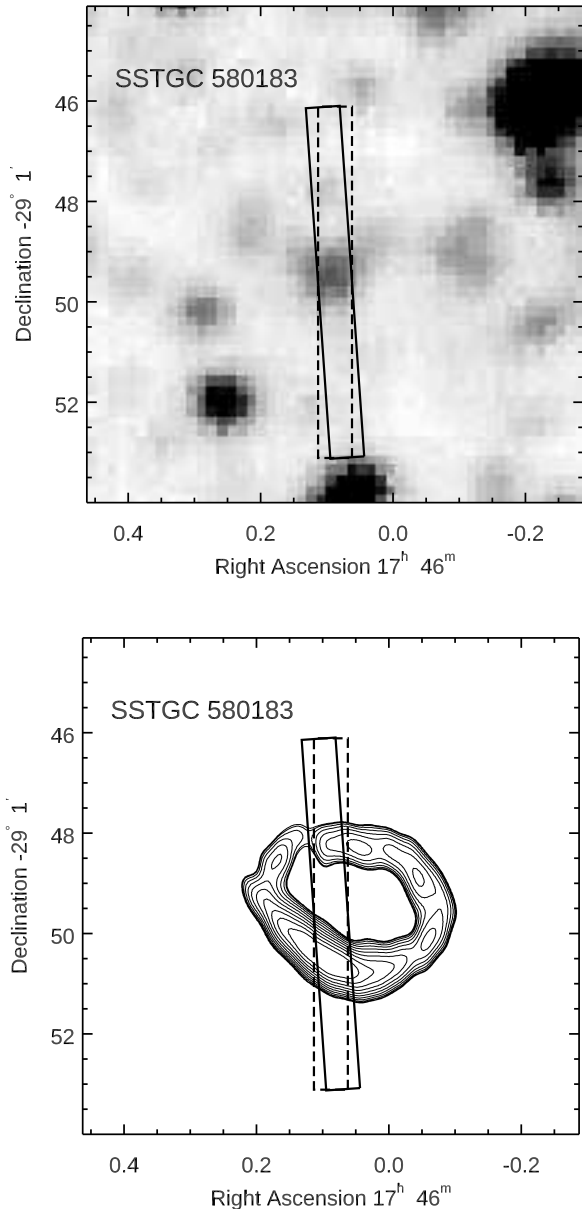


**Figure 3.** The UKIDSS  $K$ -band image (Lawrence et al. 2007, top) and the JVLA 5.5 GHz contour plot (Zhao et al. 2020, bottom) of SSTGC 580183. The GNIRS slit is overlaid on top of each image. The dashed and solid lines indicate a slit position/angle on March 11 and April 16 in 2016, respectively. North is to the top, and east to the left.

300 sec each night. We began reducing GNIRS data by removing pattern noise and flat-field correction using the

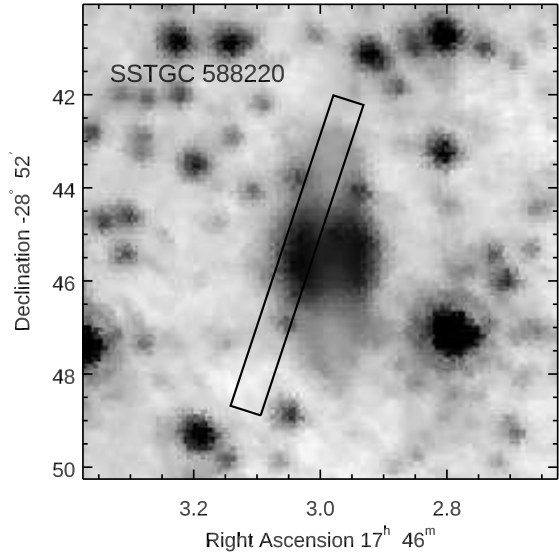


**Figure 4.** *HST*/NICMOS Paschen  $\alpha$  (F187) image (Wang et al. 2010) of SSTGC 588220. North is to the top, and east to the left. The long rectangle indicates the location of the slit on 19 March 2016.

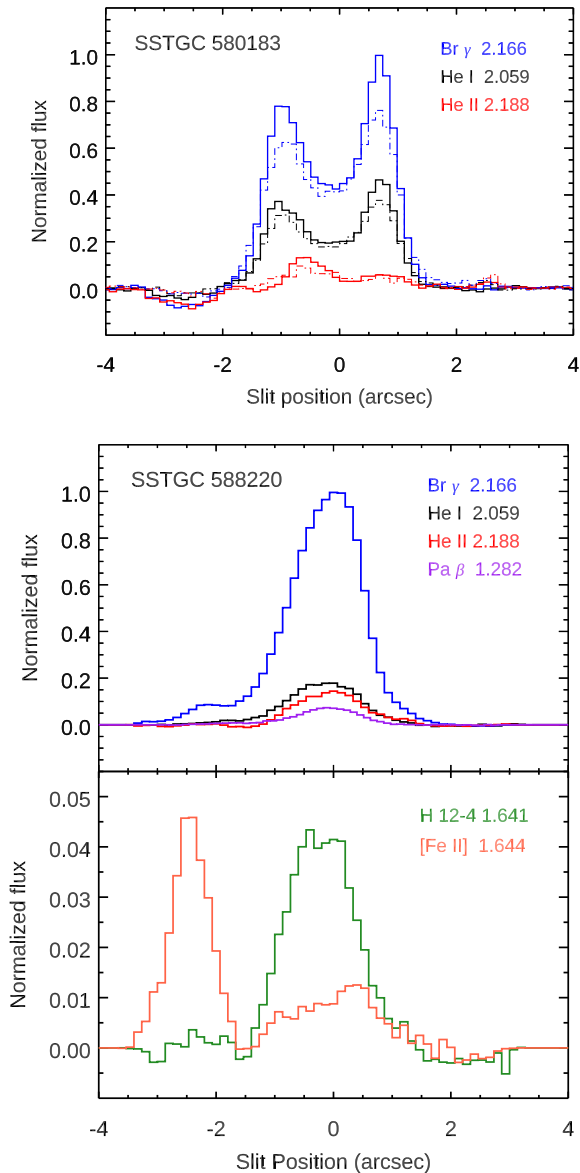
Gemini IRAF packages<sup>2</sup>. For each set of data frames, we adjusted bias levels by matching median values of pixels between spectral orders. We then followed the standard data reduction procedure for GNIRS<sup>3</sup> to correct for the order distortion, and perform wavelength calibration.

Figure 5 shows source profiles along the slit. For SSTGC 580183 (top panel), a striking bimodal structure is seen in the line emission profiles; we attribute this to the ring-like morphology observed in the radio image (see the bottom panel of Figure 3). The bimodal structures in strong lines, such as Br  $\gamma$  and H I 7–4 (2.166  $\mu\text{m}$ ), are similar, and are also seen in the weaker lines, although to a lesser degree. To collect light from the entire line emission structure, we used a 4.2''-wide aperture for spectral extraction.

On the other hand, SSTGC 588220 (middle and bottom panels of Figure 5) shows a single peak, although the slit contained extended emission and its dispersion is larger than the seeing (FWHM  $\sim$  0.6''–0.7''). Most notably, [Fe II] 1.644  $\mu\text{m}$  from SSTGC 588220 is significantly brighter in the northern ring, and is displaced by  $\sim$  2.5'' from the central emission (bottom panel). Other lines also show emission at the location of the northern

<sup>2</sup> IRAF is distributed by the National Optical Astronomy Observatory, which is operated by the Association of Universities for Research in Astronomy (AURA) under a cooperative agreement with the National Science Foundation.

<sup>3</sup> <https://www.gemini.edu/instrumentation/gnirs/data-reduction>



**Figure 5.** A flux distribution of individual lines along the slit for SSTGC 580183 (top) and SSTGC 588220 (middle and bottom). Line fluxes summed over  $6 \text{ \AA}$  are normalized with respect to the maximum value of Br  $\gamma$  emission. The dot-dashed and solid lines in the top panel show line fluxes from the first and the second run on this target, respectively. North is to the left.

ring, but its strength is significantly weaker than the one observed in the slit center. We used a  $3.6''$  aperture to extract the spectra, collecting both the central emission and the emission from the northern ring. For [Fe II], the emission line spectrum was extracted at the place where the line emission is strongest. We corrected for telluric absorptions using the Spectral Extraction Tool

**Table 1.** Line Flux Measurements from GNIRS Spectra

Line	Flux ( $10^{-15} \text{ erg s}^{-1} \text{ cm}^{-2}$ )		
	Wavelength ( $\mu\text{m}$ )	SSTGC 580183	SSTGC 588220
He I	1.0833	< 0.256	$5.311 \pm 0.078$
Pa $\beta$	1.2822	< 0.256	$6.423 \pm 0.099$
Br 12-4	1.6412	< 0.256	$1.405 \pm 0.038$
[Fe II]	1.6440	< 0.256	$1.049 \pm 0.212$
H <sub>2</sub> 1-0 S(2)	2.0338	< 0.256	$0.201 \pm 0.045$
He I	2.0587	$6.140 \pm 0.389$	$10.413 \pm 0.057$
He I	2.1128	$0.387 \pm 0.020$	$1.178 \pm 0.051$
He I	2.1137	< 0.256	$0.663 \pm 0.223$
H <sub>2</sub> 1-0 S(1)	2.1218	$0.145 \pm 0.059$	$0.738 \pm 0.045$
He I	2.1615	< 0.256	$0.719 \pm 0.049$
He I	2.1649	$0.626 \pm 0.041$	$2.339 \pm 0.201$
Br $\gamma$	2.1661	$8.370 \pm 0.395$	$31.395 \pm 0.443$
He II	2.1884	$0.252 \pm 0.022$	$3.143 \pm 0.044$
[Kr III]	2.1990	$0.249 \pm 0.112$	$0.403 \pm 0.037$
$\langle v_r^{\text{helio}} \rangle$		$+62 \pm 2 \text{ km s}^{-1}$	$-160 \pm 9 \text{ km s}^{-1}$
$\langle v_r^{\text{LSR}} \rangle$		$+72 \pm 2 \text{ km s}^{-1}$	$-150 \pm 9 \text{ km s}^{-1}$

NOTE—Upper limits are shown as a  $3\sigma$  detection limit.

(Spextool; Cushing et al. 2004) v4.1, based on nightly observation of the telluric standard star (HD 157918).

### 3. RESULTS

#### 3.1. Line Flux Measurements

Our GNIRS spectra of SSTGC 580183 and SSTGC 588220 are shown in Figures 6 and 7, respectively. The observed spectra contain several hydrogen and helium recombination lines, as well as [Fe II]  $1.644 \mu\text{m}$ , [Kr III]  $2.199 \mu\text{m}$ , H<sub>2</sub> 1-0 S(1)  $2.1218 \mu\text{m}$ , and S(2)  $2.0338 \mu\text{m}$ . Among these, Br  $\gamma$  ( $2.166 \mu\text{m}$ ) and Pa  $\beta$  ( $1.282 \mu\text{m}$ ) are of particular importance in this study, since they provide a strong constraint on the amount of foreground extinction toward each object. For SSTGC 580183, only the  $K$ -band spectrum from the highest order is shown, because most lines are essentially undetected (see individual panels at the bottom). Even [Fe II] shows a possible absorption feature, which might reflect the widespread [Fe II] emission from the interstellar medium (ISM) around the source (see An et al. 2013; Simpson 2018). Pa  $\beta$  was detected at  $2.5\sigma$  in March, but it was not seen in the April data due to a slightly lower signal-to-noise ratio (SNR). The weak Pa  $\beta$  is indicative of its large foreground extinction (see below).

Table 1 contains the line fluxes measured from the GNIRS spectra. They were measured by fitting a Gaussian function after subtracting the local continuum using a straight line. For blended lines such as He I ( $2.165 \mu\text{m}$ ) and Br  $\gamma$ , two Gaussians were used to simultaneously fit

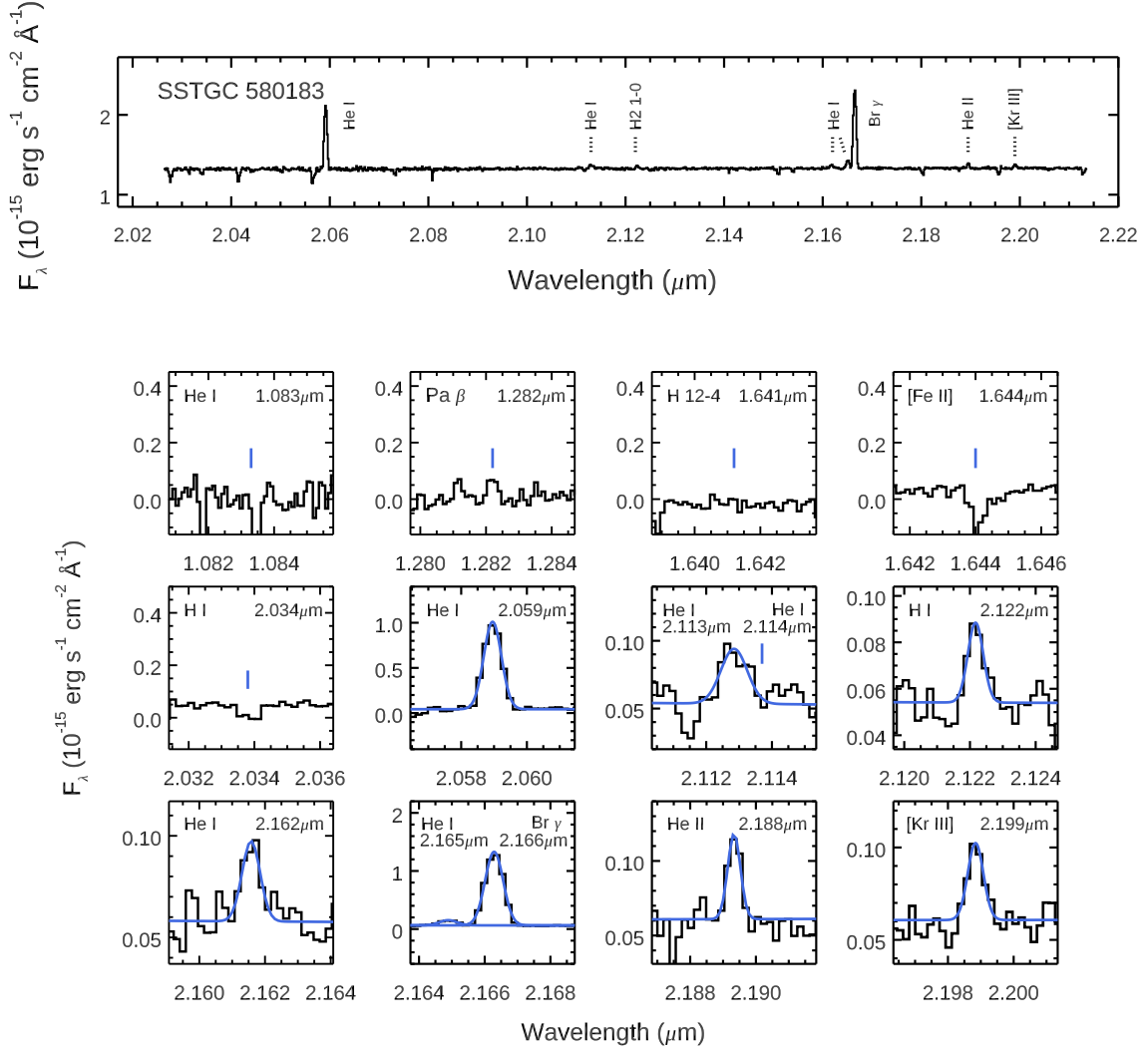


**Figure 6.** GNIRS spectra of SSTGC 580183. The other spectral orders are omitted, because none of the emission lines are detected at shorter wavelengths.

both emission lines. The uncertainties represent the difference between the best-fitting Gaussian and a direct integration of the line. A  $3\sigma$  upper limit is shown if the lines are not detected, as is the case for most of the short wavelength lines in SSTGC 580183. Heliocentric radial velocities ( $v_r^{\text{helio}}$ ) are flux-weighted, averaged values from the observed lines, and the uncertainties represent the standard deviation of these measurements. Radial velocities with respect to the Local Standard of Rest (LSR) are also given ( $v_r^{\text{LSR}}$ ).

### 3.2. Foreground Extinction Estimates

As seen from Br  $\gamma$  emission, which is stronger than Pa  $\beta$ , both objects suffer strong attenuation by a large amount of foreground dust in the Galactic disk. Such a high extinction is indicative of a large distance from the Sun, but it also means that modeling emission lines

is sensitively affected by the adopted foreground extinction. The impacts of extinction corrections on IR lines are not as significant as those required at optical wavelengths, but systematic differences in the IR extinction curves, as demonstrated below, and patchy extinction toward the CMZ generally make extinction corrections difficult.

Table 2 lists individual extinction estimates from the observed Br  $\gamma$  and Pa  $\beta$  lines for each object, based on three near-IR extinction curves (Chiar & Tielens 2006; Boogert et al. 2011; Fritz et al. 2011). For the estimate derived from Chiar & Tielens (2006), we employed their extinction curve in the line of sight to the GC. The  $3\sigma$  upper limit on Pa  $\beta$  was used to constrain the foreground extinction toward SSTGC 580183. We assumed the Case B emissivity ratios from Storey & Hummer (1995),  $j(\text{Pa } \beta)/j(\text{Br } \gamma) = 5.875$ , at a typical neb-

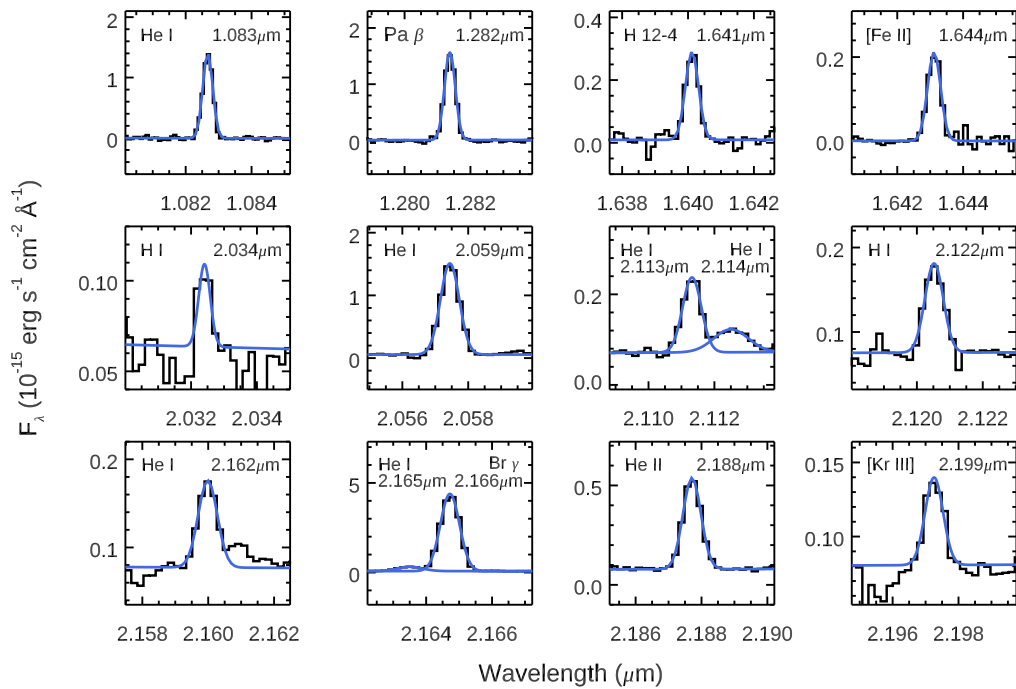
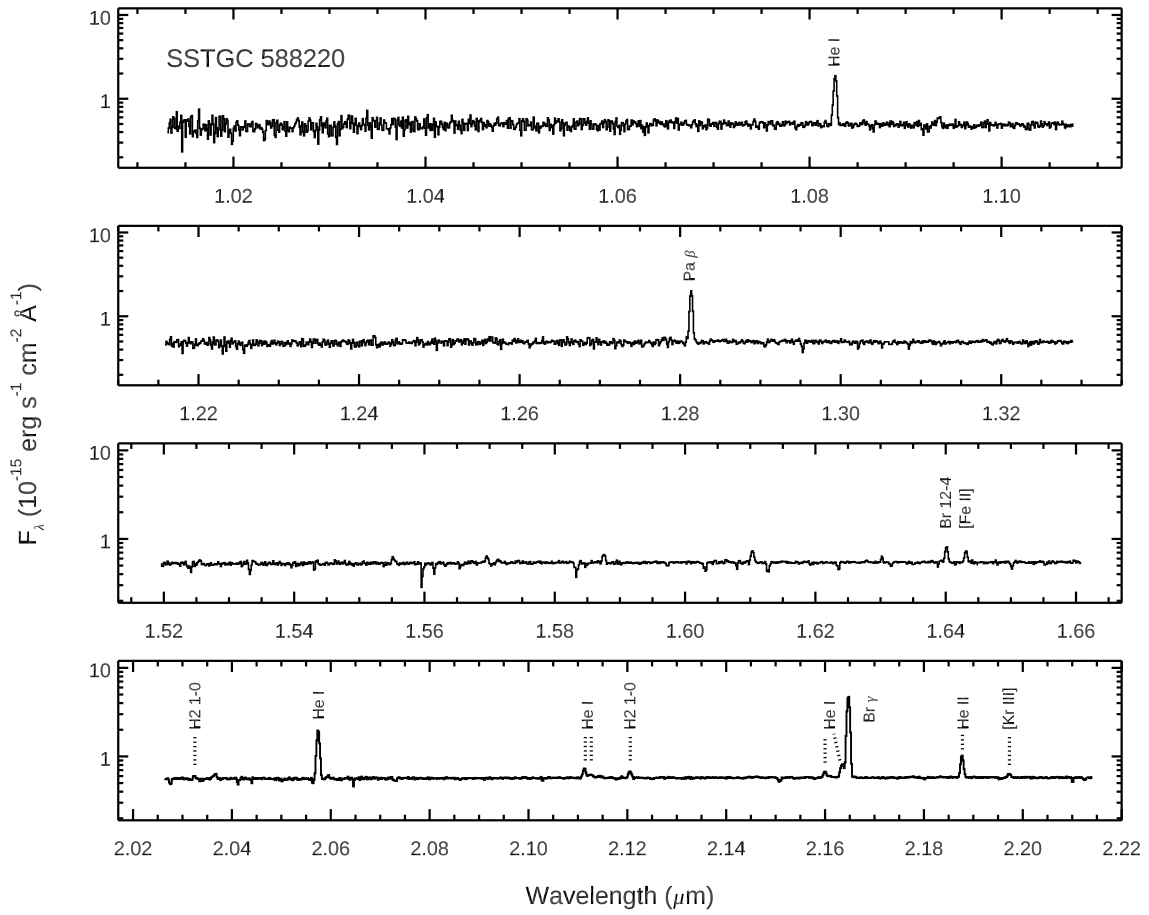


Figure 7. GNIRS spectra of SSTGC 588220.



**Table 2.** Foreground Extinction Estimates

Extinction	SSTGC 580183 <sup>a</sup>	SSTGC 588220
$A_K$ (Fritz et al. 2011)	> 2.72	$1.74 \pm 0.03$
$A_K$ (Chiar & Tielens 2006)	> 3.64	$2.33 \pm 0.04$
$A_K$ (Boogert et al. 2011)	> 3.95	$2.53 \pm 0.05$
Weighted average $\langle A_K \rangle$	> 3.26	$2.09 \pm 0.48$
Weighted average $\langle A_V \rangle^b$	> 29.7	$19.0 \pm 4.4$
$\langle \tau_{9.6} \rangle^c$	> 5.06	$3.24 \pm 0.71$
$\langle A_K \rangle$ (Schultheis et al. 2009) <sup>d</sup>	$3.76 \pm 0.49$	$2.90 \pm 0.17$
$\langle \tau_{9.6} \rangle$ (An et al. 2013) <sup>e</sup>	$2.89 \pm 0.37$	$3.69 \pm 0.31$

<sup>a</sup>  $3\sigma$  upper limits.

<sup>b</sup> Assuming  $A_K/A_V = 0.11$  (Figer et al. 1999).

<sup>c</sup> Assuming  $1.3 \leq \tau_{9.6}/A_K \leq 1.8$  (see text).

<sup>d</sup> Extinction within  $2'$  from the source.

<sup>e</sup> Extinction within  $0.9'$ – $1.5'$  from the source.

ular electron temperature ( $T_e = 10^4$  K) and density ( $n_e = 10^3 \text{ cm}^{-3}$ ) (e.g., Zhang et al. 2004) and compared them to observed line ratios to derive the extinction at  $2.2 \mu\text{m}$ ,  $A_K$ . The uncertainties are the quadratic sum of propagated values from flux measurement uncertainties and systematic differences from other Case B conditions ( $2 \times 10^3 \leq T_e \leq 2 \times 10^4$  K and  $10^2 \leq n_e \leq 10^4 \text{ cm}^{-3}$ ).

As shown in Table 2, all of the three extinction curves produce large  $A_K$  for both objects, as expected from the observed Br  $\gamma$  and Pa  $\beta$  line ratios. However, the exact values of the foreground extinction strongly depend on the adopted extinction curve. In particular, the curve of Fritz et al. (2011) has the largest slope in the near-IR among the three curves, which results in a systematically smaller  $A_K$  almost by  $\sim 30\%$ . The differences among the three extinction laws exceed the observational uncertainties.

Nevertheless, the above extinction estimates for SSTGC 588220 are smaller than the *mean* extinction toward sources in the CMZ. The average foreground extinction toward the CMZ is  $\langle A_V \rangle \approx 30$  mag, or  $\langle A_K \rangle \approx 3.3$  mag, if  $A_K/A_V = 0.11$  is adopted (Figer et al. 1999). The  $A_K$  from Fritz et al. (2011) is almost a factor of two lower than this average. In case of SSTGC 580183, where we used a  $3\sigma$  upper limit on Pa  $\beta$ , the foreground extinction estimates are slightly larger than the GC average, except from the Fritz et al. curve.

In Table 2, *local* values of the mean foreground extinction are also included. Schultheis et al. (2009) provided an extinction map across the CMZ, based on IR colors of red giant branch stars in a grid of  $2' \times 2'$ . The  $A_K$  represents the mean and standard deviation of their measurements within  $2'$  from each source. Taking

$A_K/A_V = 0.11$ , their estimates correspond to  $A_V \sim 30$ – $40$ , which is consistent with the average extinction toward the GC. While the Schultheis et al. (2009) map represents the bulk average of foreground extinction toward each source, An et al. (2013) provided local extinction that is more specific to their lines of sight. In practice, An et al. (2013) followed the procedure in Simpson et al. (2007), and estimated the optical depth at  $9.6 \mu\text{m}$  ( $\tau_{9.6}$ ) from the flux ratio between  $10 \mu\text{m}$  and  $14 \mu\text{m}$ , measuring the strength of the silicate absorption band centered at  $9.6 \mu\text{m}$  (see also Simpson 2018). The  $\langle \tau_{9.6} \rangle$  and its uncertainty are the average and standard deviation from four nearby (within  $0.9'$ – $1.5'$ ) *Spitzer*/IRS slits that were originally designed to measure background CMZ emissions (An et al. 2009, 2011).

In contrast, Simpson (2018) estimated values of  $\tau_{9.6} = 2.725$  for SSTGC 580183 and  $2.803$  for SSTGC 588220, using a combination of the shapes of the  $10 \mu\text{m}$  silicate feature and the [S III]  $18.7 \mu\text{m}/33.5 \mu\text{m}$  line ratios. We emphasize that these extinction values, like those from An et al. (2013), apply to the diffuse ISM in the GC and not to objects much smaller than the *Spitzer* IRS apertures that may be substantially in front of (or behind) the CMZ of the GC.

The conversion between  $A_K$  and  $\tau_{9.6}$  also depends on the shape of the extinction curve over the wavelength interval. If  $A_V/\tau_{9.6} = 9$  (Roche & Aitken 1985) is taken, along with  $A_K/A_V = 0.11$ ,  $\tau_{9.6}/A_K$  becomes unity. On the other hand, the two extinction curves employed in this work predict  $\tau_{9.6}/A_K = 1.3$  (Chiar & Tielens 2006) and  $1.8$  (Fritz et al. 2011), implying relatively strong silicate absorption with respect to  $A_K$ . In Table 2,  $\langle \tau_{9.6} \rangle$  is the mean from the two cases with Chiar & Tielens (2006) and Fritz et al. (2011) laws, while the uncertainty indicates half of the difference. The  $\tau_{9.6}$  estimates from GNIRS spectra are  $15\%$ – $20\%$  smaller than the ISM extinction measurements from An et al. (2013), implying that the source is likely located in front of gas and dust in the CMZ. Taking these at face value, the larger  $A_K$  from background giants (Schultheis et al. 2009) also implies a shorter distance to SSTGC 588220 than the GC. In case of SSTGC 580183, the  $3\sigma$  upper limits are comparable to the foreground extinction from Schultheis et al. (2009), while they are higher than the An et al. (2013) estimates.

### 3.3. Comparison to the Size versus Surface Brightness Relations of PNe

Galactic and extra-Galactic PNe exhibit a tight correlation between the radius and surface brightness (e.g., Frew et al. 2016b; Stanghellini et al. 2020, see Figures 8 and 9), according to which a smaller PN tends to have

a higher mean surface brightness. Because other astrophysical nebulae, such as classical nova shells, show noticeable offsets from this relation (e.g., Frew et al. 2016a), its direct comparison can be used not only to confirm the nature of our sources as PNe, but also to constrain a distance range assuming that our sources directly follow the mean PN relation.

For this comparison, we measured an angular size of SSTGC 588220 from the *HST*/NICMOS Pa  $\alpha$  image (Wang et al. 2010). Since the bright inner rim shows a mild ellipticity (Figure 4), we took an average of the angular diameter measured along the major and minor axes,  $2.83 \pm 0.02''$ . Reassuringly, this size is comparable to the spatial extent of the observed emission line profiles (Figure 5). On the other hand, emission lines from SSTGC 580183 show double peaks along the slit, and the observed full extent is approximately equal to the mean diameter from high-resolution radio images (Zhao et al. 2020),  $3.86 \pm 0.04''$ .

For our targets, the H $\alpha$  and H $\beta$  fluxes were computed from the extinction-corrected Br  $\gamma$  line flux, assuming the same Case B recombination coefficients as in the previous section:  $j(\text{H}\alpha)/j(\text{Br}\gamma) = 103.0$  and  $j(\text{H}\beta)/j(\text{Br}\gamma) = 36.1$  (Storey & Hummer 1995). For the uncertainty estimates, we considered a range of these coefficients over  $5 \times 10^3 \leq T_e(K) \leq 2 \times 10^4$  and  $10^2 \leq \log N_e \leq 10^4$  (92.2–118 and 30.3–43.0, respectively). Because the foreground extinction was computed from the line ratio between Br  $\gamma$  and Pa  $\beta$ , the H $\alpha$  and H $\beta$  line fluxes depend on which of the three extinction curves included in this study is taken; therefore, we explicitly included it as a source of the systematic uncertainties. Since the GNIRS targets are more extended than the slit width, we estimated the amount of light lost by simulating our observations with the continuum-subtracted *HST* Pa  $\alpha$  images (Wang et al. 2010). From this, we found that the  $0.675''$ -wide slit collects approximately  $41\% \pm 3\%$  of the total light from SSTGC 588220. In case of SSTGC 580183, we used the 5.5 GHz map in Zhao et al. (2020) to compute the surface area covered by the slit,  $18\% \pm 4\%$ , assuming a 20% uncertainty in this measurement.

Figure 8 shows the radius versus H $\beta$  surface brightness relation of the Galactic PNe in Stanghellini et al. (2020), which is based on accurate distances to PNe central stars from *Gaia* DR2 (Gaia Collaboration et al. 2018). A comparison to our GNIRS observation for SSTGC 580183 is shown in the top, and SSTGC 588220 in the bottom panel, assuming that they are located in the GC at a distance of 8.2 kpc (Gravity Collaboration et al. 2019; Reid et al. 2019). In both panels, the average H $\beta$  surface brightness esti-

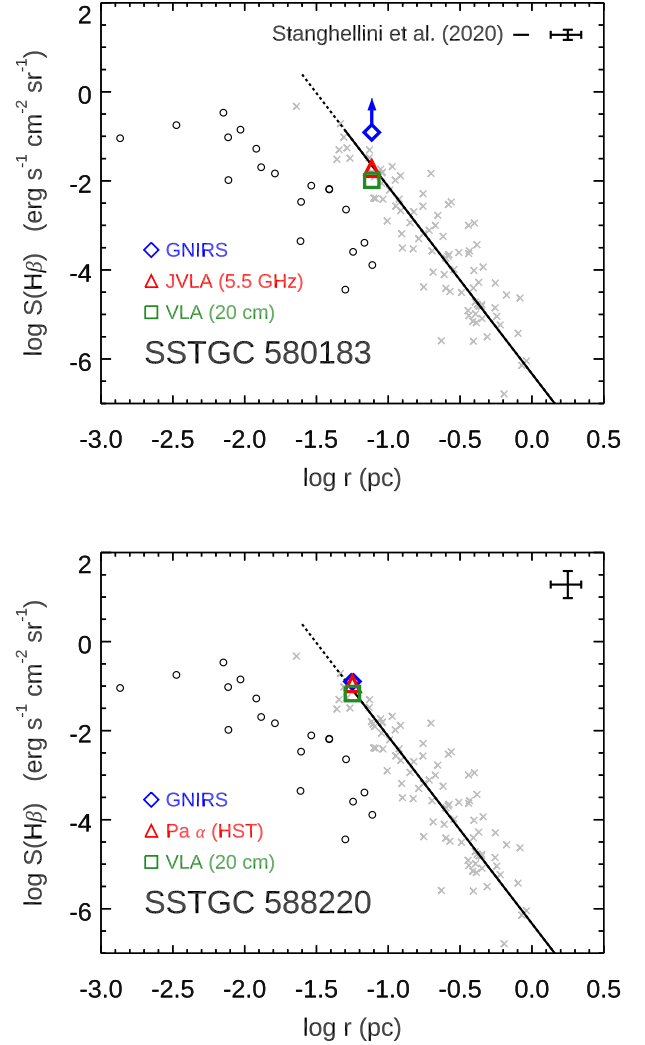


**Figure 8.** Comparisons of SSTGC 580183 (top) and SSTGC 588220 (bottom) to the radius versus H $\beta$  surface brightness relation of PNe in Stanghellini et al. (2020). The surface brightness estimates from GNIRS observations are indicated by the blue open diamonds. Other measurements from JVLA 5.5 GHz (Zhao et al. 2020, red triangle in the top), VLA 20 cm (Yusef-Zadeh et al. 2004, green boxes), and *HST* Pa  $\alpha$  observations (Wang et al. 2010, red triangle in the bottom) are also shown assuming that the sources are located at the GC distance (8.2 kpc). Representative error bars are shown with a range of  $\pm 2$  kpc. The GNIRS-based estimate for SSTGC 580183 indicates a  $3\sigma$  lower limit. The grey crosses are Galactic PNe in Stanghellini et al. (2020), and the open circles indicate a subset of these with low ionized mass (see their Figure 3); their best-fitting power law is shown by a solid line, and its extrapolation beyond the sample limit is indicated by a dotted line.

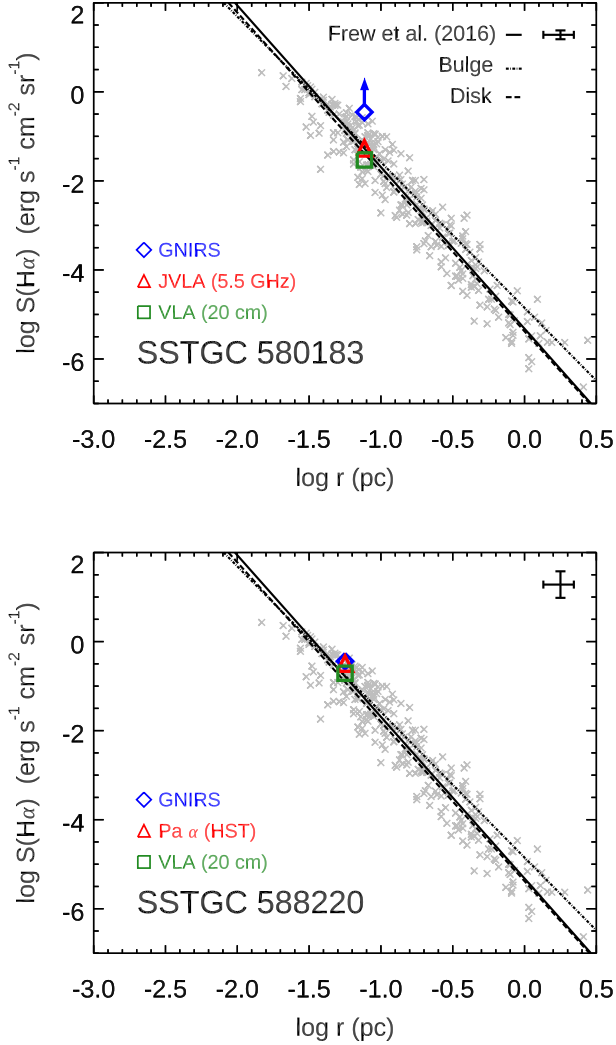


**Figure 9.** Same as in Figure 8, but showing comparisons to the radius versus  $H\alpha$  surface brightness relation in Frew et al. (2016b). The relations derived from Galactic bulge and disk populations are indicated by the dotted and dashed lines, respectively. The best-fitting power law of their full calibrator sample is shown by a solid line.

mated from the GNIRS  $\text{Br } \gamma$  flux is shown by blue open diamonds, assuming an average extinction toward each object (Table 2). Since the lower limit on the extinction correction is available for SSTGC 580183, its  $3\sigma$  lower limit is marked. The vertical error bars indicate the quadrature sum of the uncertainties from the flux measurements, extinction corrections, Case B emissivities, and a 20% uncertainty in the absolute flux calibration. The horizontal error bars indicate a range of a physical radius, assuming  $\pm 2$  kpc differences from the GC distance.

The grey crosses in Figure 8 indicate individual Galactic PNe in Stanghellini et al. (2020). There is a significant scatter of points below the relation at smaller radii, which is attributed to the low ionized masses ( $< 0.01 M_{\odot}$ ) of these objects among other possible causes (see discussions in Stanghellini et al. 2020). Accordingly, if our candidate PNe do not follow the mean size versus surface brightness relation, but are outliers with systematically smaller radii, the inferred distances would become significantly larger by an order of magnitude. However, the ionized masses of SSTGC 580183 and SSTGC 588220 based on radio fluxes ( $\sim 0.4\text{--}3 M_{\odot}$  assuming 4–8 kpc distances) are larger than the upper limit for their outliers, rejecting such hypothesis. The solid line shows the best-fitting relation to the data in Stanghellini et al. (2020) without the low-ionized mass sample.

In addition, Figure 9 shows comparisons to the size versus  $H\alpha$  surface brightness relation of the Galactic and extra-Galactic PNe of Frew et al. (2016b). The grey crosses indicate the Galactic and extra-Galactic ‘calibrator’ sample in their study, which do not show the same large scatter at small radii as in Figure 8. The black solid line indicates their best-fitting relation to all sample PNe. The dotted and dashed lines show the observed relations for the bulge and disk PNe in the Milky Way, respectively, which are not significantly different from each other and from the mean relation.

In all cases, the GNIRS observations are in good agreement with the PN relations if the sources are put at the GC distance. The same conclusion can be drawn using the  $\text{Pa } \alpha$  flux measurement from *HST*/NICMOS for SSTGC 588220 (red open triangles in the bottom panels of Figures 8 and 9). As an independent check on these results, we also employed radio continuum fluxes from VLA 20 cm (Yusef-Zadeh et al. 2004) and JVLA 5.5 GHz observations (Zhao et al. 2020) to infer their  $H\alpha$  and  $H\beta$  surface brightnesses, which are essentially free of extinction errors. Moreover, the radio images encompass the whole structure of each target and therefore do not need slit-loss corrections. We employed the relation between the hydrogen recombination line flux and the free-free emission in Scoville et al. (2003) and assumed the same set of recombination line Case B emissivities as in the previous section. The surface brightness estimates derived from radio fluxes are marked by green boxes (VLA 20 cm) and red triangles (JVLA 5.5 GHz; top panels) in Figures 8 and 9, which show a good agreement with both Frew et al. (2016b) and Stanghellini et al. (2020) relations.

Assuming that our candidate PNe follow the surface brightness versus radius relations in the above two stud-

**Table 3.** Heliocentric Distance Estimates

Observations/Relation <sup>a</sup>	SSTGC 580183	SSTGC 588220
Br $\gamma$ /Frew et al.	< 4.8 kpc	$6.5 \pm 1.8$ kpc
Br $\gamma$ /Stanghellini et al.	< 5.5 kpc	$7.4 \pm 1.5$ kpc
Pa $\alpha$ /Frew et al.	...	$6.7 \pm 1.8$ kpc
Pa $\alpha$ /Stanghellini et al.	...	$7.6 \pm 1.5$ kpc
20 cm/Frew et al.	$9.5 \pm 1.5$ kpc	$7.7 \pm 1.4$ kpc
20 cm/Stanghellini et al.	$9.9 \pm 2.1$ kpc	$8.6 \pm 1.9$ kpc
5.5 Ghz/Frew et al.	$8.1 \pm 1.3$ kpc	...
5.5 Ghz/Stanghellini et al.	$8.6 \pm 1.8$ kpc	...
Average	$9.0 \pm 1.6$ kpc <sup>b</sup>	$7.6 \pm 1.6$ kpc

<sup>a</sup> Observations: wavelengths at which fluxes were measured to derive surface brightness – Br  $\gamma$  (this study), Pa  $\alpha$  (Wang et al. 2010), 20 cm (Yusef-Zadeh et al. 2004), and 5.5 GHz (Zhao et al. 2020). Relations: surface brightness versus size relations of PNe in Frew et al. (2016b) and Stanghellini et al. (2020) to compute a physical size of a PN.

<sup>b</sup> An weighted average distance from radio observations.

ies, we proceed to constrain the range of distance to each object by directly comparing its measured angular size to the inferred physical size for the estimated average surface brightness. The heliocentric distances computed in this way are summarized in Table 3. The first two rows show distance estimates using the Br  $\gamma$  fluxes measured with GNIRS in this study, based on Frew et al. (2016b) and Stanghellini et al. (2020), respectively. For SSTGC 580183, upper distance limits are shown from the lower limit in the foreground extinction. The uncertainties include those propagated from the surface brightness measurements and the fitting coefficients in each of the relations. Within the uncertainties, both PN relations give consistent distance estimates with each other for each PN candidate.

As shown in Table 3, the distances to SSTGC 588220 derived from the near-IR line fluxes are slightly smaller than those estimated using radio flux measurements, although they are in mutual agreement within the estimated uncertainties. On the other hand, the  $3\sigma$  upper distance limits for SSTGC 580183 seem too small compared to those derived from radio fluxes. This implies that our estimated foreground extinction toward SSTGC 580183 may be too large, or that there may be systematic errors in the adopted extinction curves. The average distance to SSTGC 580183 in Table 3 indicates a mean distance from radio observations; an average distance to SSTGC 588220 is derived from near-IR and radio observations. These average distances, as well as high foreground extinction, indicate that both targets are likely located in the central region of the Milky Way.

#### 4. NEBULAR ABUNDANCES

**Table 4.** Physical Parameters used in the Cloudy Models

	SSTGC 580183	SSTGC 588220
$T_{\text{eff}}$ (K) <sup>a</sup>	108, 555	133, 278
Log Q(H) ( $\text{s}^{-1}$ )	46.892	47.194
Inner Radius (pc)	0.0500	0.02235
Electron Density ( $N_e$ ; $\text{cm}^{-3}$ )	$5550 \pm 2300$	$1602 \pm 813$
Hydrogen Density ( $N_H$ ; $\text{cm}^{-3}$ )	3945	3023
Filling Factor ( $f$ )	0.1000	0.2857

<sup>a</sup> Effective temperature of an ionizing star from stellar atmosphere models at  $\log g = 6$  (Rauch 2003).

#### 4.1. Cloudy Models

Estimates were made of the abundances of the two candidate PNe using Cloudy 17.02 (Ferland et al. 2017). The input parameters to the Cloudy models are summarized in Table 4. These include the effective temperature ( $T_{\text{eff}}$ ) of the exciting star (here,  $\log g = 6$  white dwarf models at solar abundance taken from Rauch (2003)), the hydrogen nucleus density  $N_H$  (the electron density  $N_e$  being variable with depth in the models depending on the local ionization of the multi-electron elements), the filling factor  $f$  (see Simpson (2018) for equations relating  $N_H$  and  $f$ ), and the abundances of helium and the heavy elements (see below). The total ionizing luminosities  $Q(\text{H})$  (number of photons  $\text{s}^{-1}$ ) were estimated from the radio fluxes measured by Zhao et al. (2020) for SSTGC 580183 and by Yusef-Zadeh et al. (2004) for SSTGC 588220, with the assumption of a rounded GC distance of 8 kpc,  $T_e = 10^4$  K, and the use of Equation (1) of Simpson & Rubin (1990). The inner radii were measured from Figures 3 and 4, and were scaled at 8 kpc. We note that, since all model comparisons are made using line flux ratios, the model results will not change if the estimated distances are different from 8 kpc.

In this modeling effort, we included various mid-IR lines measured with the *Spitzer* IRS, in addition to the hydrogen and helium lines observed with GNIRS. We utilized the line intensity measurements from Simpson (2018), which were based on the spectral extraction tool CUBISM (Smith et al. 2007) with point-source flux calibration. All of the lines were measured by fitting Gaussians to the spectra. Some lines were re-measured in this study using the IRS analysis program SMART-IDEA (Higdon et al. 2004) for better accuracy. These include [S IV] 10.51  $\mu\text{m}$ , [Ar V] 13.10  $\mu\text{m}$ , [Mg V] 13.52  $\mu\text{m}$ , [Fe VI] 14.77  $\mu\text{m}$ , [P III] 17.88  $\mu\text{m}$ , [Fe II] 17.94  $\mu\text{m}$ , [Ar III] 21.83  $\mu\text{m}$ , [Ne V] 24.32  $\mu\text{m}$ , and [Fe III] 22.93  $\mu\text{m}$ . As described in § 2, background subtraction was performed on a line-by-line basis by taking the aver-

age of high-resolution (IRS SH and LH modules) fluxes at four nearby positions, while for the low-resolution modules (SL and LL), background positions were measured from slightly distant positions along the same slits.

In Table 5, the extinction-corrected line fluxes are expressed as line ratios with respect to the hydrogen recombination lines, where H I 7–4 (Br  $\gamma$ ) was used for those observed with GNIRS, and H I 7–6 (12.37  $\mu\text{m}$ ) for the IRS observations. The division into two wavelength intervals was necessary to minimize systematic errors from different slit sizes – the GNIRS observations were made with a relatively narrow slit (‘slit’ models), while the longer-wavelength IRS slits were large enough to include almost the whole source (‘whole nebular’ models). We corrected the observed near-IR line fluxes for extinction using  $A_K$  estimates derived from the Fritz et al. (2011) extinction curve (Table 2). The same extinction curve was used for mid-IR emission lines up to the peak of the 9.7  $\mu\text{m}$  silicate feature. At longer wavelengths, however, we employed the Chiar & Tielens (2006) extinction curve because it extends to a longer wavelength ( $\sim 35$   $\mu\text{m}$  instead of the 27  $\mu\text{m}$  of Fritz et al. (2011)). Also, it is based on a source that should have absorption only (the Quintuplet Cluster star GCS 3) and not a source for which one must compensate for dust emission (Sgr A) in the extinction curve estimate at the longest wavelengths (Fritz et al. 2011). The uncertainties in the background-subtracted line intensities include uncertainties from the flux measurements and the background subtraction, which are added in quadrature.

For the reasons described above, we performed separate Cloudy runs to account for the ‘slit’ models and the ‘whole-nebula’ models. In the former, the near-IR lines Br  $\gamma$ , He I 2.059  $\mu\text{m}$ , and He II 2.189  $\mu\text{m}$  lines were used to produce estimates of  $T_{\text{eff}}$  and the He/H ratio.<sup>4</sup> In the whole-nebula integrated models, the mid-IR lines were used to produce estimates of  $N_{\text{H}}$  and  $f$  for SSTGC 588220.

We used Cloudy with its ‘optimize’ commands, where, in each call, a given parameter or a set of parameters is allowed to vary with the best solution based on the deviation of the model predictions for a set of lines with the observed fluxes. Because of the large number of input parameters, relative to limited observational information, a uniform density and a constant filling factor were assumed in these models. The elemental abundances were fit by hand by comparing the model output

with the observed line flux ratios. The filling factor was computed by ‘optimize’ command for SSTGC 588220, but this was not successful for SSTGC 580183. Instead, models with a variety of filling factors were computed and the median model with  $f = 0.10$  was selected.

Elemental abundances in the models, other than those derived in the modeling, were taken from Cloudy’s standard set for an H II region, nominally that of the Orion Nebula. The abundances of carbon, nitrogen, and silicon were set to the GC abundance ratios with respect to oxygen in Simpson (2018): C/O=0.75, N/O=0.17, and Si/O=0.035. This allows for some depletion into grains, whose opacities are included in the calculation.

Criteria for an acceptable fit and steps in the modeling process are:

(i) The He II 2.189  $\mu\text{m}$ /He I 2.059  $\mu\text{m}$  line ratio, which is used to estimate  $T_{\text{eff}}$  of the PN central star, should be equal to the observed ratio. Iteration was needed, since the exact  $T_{\text{eff}}$  is somewhat dependent on  $N_{\text{H}}$  and  $f$  as they both affect the ionization parameter  $U$  (Simpson 2018, see their Equation 2).

(ii) The density-sensitive line pairs (mainly [S III] 18.7  $\mu\text{m}$  and 33.5  $\mu\text{m}$ , but also [Ne V] 14.3  $\mu\text{m}$  and 24.3  $\mu\text{m}$  for SSTGC 588220) should agree with the observed line ratios; the [Ar III] 8.99  $\mu\text{m}$  and 21.8  $\mu\text{m}$  line pair in SSTGC 580183 was not used because of their large uncertainties. As shown in the high-resolution images (bottom panel of Figures 3 and 4), the PNe may not have a constant density. Indeed, it was not possible to find constant density models that produce line ratios that agree with all line pairs. For this reason, less weight was given to the [S III] line pair in SSTGC 588220, which has larger uncertainties than the [Ne V] line pair.

(iii) The line ratios with respect to hydrogen should agree with the observed ratios. To assure this, the relative abundances of helium and the heavy elements were adjusted in each iteration. In the models, the abundances of carbon, nitrogen, and silicon, all unobserved in our candidate PNe, were scaled to the abundance of oxygen according to the H II region abundances used by Simpson (2018). This resulted in additional iterations as changing the abundances modifies the cooling function and hence the electron temperature, which in turn affects all computed fluxes and flux ratios.

#### 4.2. Results

The elemental abundances in the best-fitting Cloudy models are given in Table 6. Although we ran models assuming constant  $N_{\text{H}}$  and  $f$ , the above modeling exercise provides useful and reliable information on the central star  $T_{\text{eff}}$  and, in particular, the abundances of helium, neon, and sulfur, all of which were observed in lines

<sup>4</sup> The other  $K$ -band He I lines are listed here by their most important components, but are actually blends with lines that are distinguished in Cloudy. We are unable to separate them owing to the moderate spectral resolution of our data.

**Table 5.** Normalized Line Fluxes

Emission Line	Wavelength ( $\mu\text{m}$ )	SSTGC 580183 (G359.963–0.120)				SSTGC 588220 (G0.098–0.051)			
		Observation		Model		Observation		Model	
		Flux <sup>a</sup>	Uncertainty <sup>b</sup>	Flux <sup>c</sup>	Ion. <sup>d</sup>	Flux <sup>a</sup>	Uncertainty <sup>b</sup>	Flux <sup>c</sup>	Ion. <sup>d</sup>
<i>Gemini GNIRS (slit models)</i>									
Paschen beta	1.2822	...	...	...	...	5.877	0.015	5.577	–0.028
Brackett 12–4	1.6412	...	...	...	...	0.168	0.031	0.186	–0.028
Brackett gamma	2.1661	1.000	0.047	1.000	–0.053	1.000	0.014	1.000	–0.028
He I $2^3P-2^3S$	1.0833	...	...	...	...	40.445	0.020	8.427	–0.214
He I $2^1P-2^1S$	2.0587	0.9846	0.079	0.9847	–0.050	0.4003	0.015	0.3997	–0.214
He I $4^3P-3^3S$	2.1128	0.0532	0.070	0.0382	–0.050	0.041	0.046	0.016	–0.214
He I $4^1P-3^1S$	2.1137	...	...	...	...	0.023	0.336	0.006	–0.214
He I $7^3F-4^3F$	2.1615	...	...	...	...	0.023	0.070	0.011	–0.214
He I $7^3G-4^3F$	2.1649	...	...	...	...	0.075	0.087	0.017	–0.214
He II 10–7	2.1884	0.0285	0.101	0.0286	–1.247	0.0966	0.020	0.0966	–0.437
[Fe II]	1.6440	...	...	...	...	0.225	0.203	11.555	–0.835
<i>Spitzer IRS (whole nebula models)</i>									
H 7–6	12.3719	1.000	0.055	1.000	–0.066	1.000	0.099	1.000	–0.040
[O IV]	25.8903	63.68	0.152	63.42	–1.765	330.95	0.102	330.58	–0.882
[Ne II]	12.8135	41.79	0.057	44.91	–0.861	15.57	0.111	28.97	–1.195
[Ne III]	15.5551	408.64	0.056	379.88	–0.075	413.37	0.099	470.68	–0.107
[Ne V]	14.3217	...	...	...	–4.897	160.13	0.099	140.39	–1.666
[Ne V]	24.3175	...	...	...	–4.897	113.35	0.099	94.50	–1.666
[Na III]	7.3169	5.36	0.077	5.35	–0.112	...	...	...	–0.154
[Mg V]	13.5213	...	...	...	–5.697	0.654	0.283	0.655	–1.757
[P III]	17.8850	0.916	0.469	0.919	–0.460	1.716	0.307	1.717	–0.412
[S III]	18.7130	120.28	0.057	107.50	–0.271	81.82	0.102	91.86	–0.294
[S III]	33.4810	36.74	0.232	32.85	–0.271	40.02	0.316	34.38	–0.294
[S IV]	10.5105	93.39	0.056	104.45	–1.069	245.80	0.099	219.05	–0.670
[Cl II]	14.3678	1.246	0.067	1.245	–0.520	...	...	...	–0.752
[Ar II]	6.9853	14.46	0.088	10.01	–1.087	...	...	...	–1.310
[Ar III]	8.9910	35.60	0.068	83.23	–0.094	...	...	...	–0.173
[Ar III]	21.8302	5.816	0.121	5.151	–0.094	4.626	0.121	2.484	–0.173
[Ar V]	13.1022	...	...	...	–2.604	6.031	0.101	11.20	–1.277
[Fe III]	22.9250	4.348	0.145	4.345	–0.530	17.67	0.110	17.65	–0.659
[Fe VI]	14.7710	...	...	...	–2.908	0.446	0.139	14.08	–1.214

<sup>a</sup> Extinction-corrected observed line fluxes with respect to Br  $\gamma$  (GNIRS) from Table 1 or H I 7–6 12.37  $\mu\text{m}$  (IRS, Simpson 2018).

<sup>b</sup> Uncertainties in the observed line flux ratios, consisting of the statistical uncertainties from the line flux measurements combined quadratically with the uncertainty of the associated hydrogen recombination line.

<sup>c</sup> Modeled line fluxes with respect to Br  $\gamma$  or H I 7–6 12.37  $\mu\text{m}$ .

<sup>d</sup> Logarithm of the fractional ionization of each ion.

from more than one ionization stage. Of lesser reliability are the elements observed from only a single ionization stage, although some have, at least, the dominant ionization stage observed. Even so, a detailed modeling of as many ionization stages as is done here can produce more reliable results than the use of estimated ionization correction factors (*ICFs*) that is otherwise common in determining nebular abundances.

The uncertainties in the background subtraction propagate into significant uncertainties in the final abundances for most of heavy elements. This is because abundances are tabulated with respect to hydrogen,

where the strongest hydrogen line in the IRS wavelength is the H 7–6 line at 12.37  $\mu\text{m}$ , which is sensitive to the background subtraction. Whereas the highest excitation lines had little or no presence in the background spectra, the low excitation lines have substantial background emission that needs to be removed. In particular, background subtraction removes 27% of the measured target flux of the H 7–6 line for SSTGC 580183, and 40% of the measured target flux for SSTGC 588220 (see Figure 2); the final SNRs are 18 and 10 for SSTGC 580183 and SSTGC 588220, respectively (Table 5). The other singly ionized lines ([Ne II], [Ar II], and [Fe II]) have even

**Table 6.** Elemental Abundances

Elements	Log Abundances <sup>a</sup>		
	SSTGC 580183	SSTGC 588220	Solar <sup>b</sup>
Hydrogen	12.00	12.00	12.00
Helium	11.09 ± 0.04	10.86 ± 0.03	[10.93]
Oxygen	9.22 ± 1.27	8.96 ± 0.80	8.69
Neon	8.56 ± 0.04	8.67 ± 0.04	[7.93]
Sodium	6.68 ± 0.06	...	6.21
Magnesium	...	8.05 ± 1.25	7.60
Phosphorus	5.68 ± 0.16	5.86 ± 0.16	5.41
Sulfur	7.48 ± 0.18	7.36 ± 0.22	7.12
Chlorine	5.62 ± 0.10	...	5.50
Argon	7.00 ± 0.04	6.72 ± 0.05	[6.40]
Iron	6.83 ± 0.19	7.52 ± 0.15	7.47
Kr <sup>c</sup>	3.99 ± 0.20	3.67 ± 0.06	[3.25]

<sup>a</sup>  $\log(N_A/N_H) + 12$ .

<sup>b</sup> Solar abundances from [Asplund et al. \(2009\)](#) with the exceptions of Na, Mg, and Fe, which are from [Scott et al. \(2015a,b\)](#). The brackets around the noble gas abundances indicate that these Solar abundances are ‘indirect photo-spheric estimates’ ([Asplund et al. 2009](#)).

<sup>c</sup> Krypton (Kr) was modeled separately from the Cloudy runs (see text).

more flux subtracted (so much so for [Fe II] that this line was dropped from the analysis), but these elements have doubly ionized lines in the IRS spectra, which make our abundance estimates more secure.

The abundance uncertainties in Table 6 are the sum, in quadrature, of the measurement uncertainty, the uncertainty due to a possible error in the extinction of  $\Delta\tau_{9.6} = 0.5$ , and an estimate of the model error expressed as the uncertainty in the *ICF*. This *ICF* uncertainty is estimated to be the value of 0.05 divided by the fractional ionization of the observed ion for elements where only one ionization state was observed or it is estimated to equal 0.25 times the fractional ionization of the unobserved ionization states when multiple ionization states were observed. Which of these errors dominates depends on the line – the measurement error is important for the two blended lines, [P III] 17.88  $\mu\text{m}$  and [Fe II] 17.94  $\mu\text{m}$  (the latter having such a large uncertainty that it was not further included); the extinction error is mainly important for the lines with wavelengths near 10  $\mu\text{m}$  and 18  $\mu\text{m}$  (this uncertainty is large because the silicate extinction curve is not that well known); and the *ICF* error dominates for lines arising from ions with very low fractional ionization, such as  $\text{O}^{3+}$  and  $\text{Mg}^{4+}$ . Finally, the uncertainty for O/H in SSTGC 588220 was increased because the line was saturated in the high-resolution IRS module (LH) and the flux had to be taken from the low-resolution (LL1) observation.

#### 4.2.1. SSTGC 588220 (G0.095-0.051)

The fluxes predicted by the Cloudy models provide a reasonably good agreement with the observed fluxes. However, in spite of the overall agreement, notable discrepancies are found in some lines. For instance, the best-fitting model over-predicts fluxes from [Ar V] 13.1  $\mu\text{m}$  and [Fe VI] 14.7  $\mu\text{m}$ , while it under-estimates the He I 1.083  $\mu\text{m}$  flux. The over-estimated high-excitation lines are probably the result of the source not being spherically symmetric and having large density fluctuations. On the other hand, the He I 1.083  $\mu\text{m}$  line is more sensitive to the amount of extinction than the longer-wavelength He lines, and its emissivity is more dependent on details of the electron density distribution than the emissivity of the He I 2.059  $\mu\text{m}$  line (see [Porter et al. 2012, 2013](#)).

#### 4.2.2. SSTGC 580183 (G359.963-0.120/G-0.037-0.120)

The agreement with the best-fitting model is less satisfactory in case of SSTGC 580183, most likely due to the PN having components of multiple densities and filling factors, rather than having constant values as assumed in the current analysis. In particular, the ‘optimize’ command in Cloudy initially produced a very low filling factor ( $f \approx 0.03$ ) in the models, driven by the absence of high ionization lines such as [Ne V], [Ar V], and [Mg V] in the *Spitzer* mid-IR spectra, except [O IV] 26  $\mu\text{m}$ . The models described in Tables 4 and 5 were produced with  $f = 0.1$  (the model parameters do not change appreciably with changing  $f$ ) and inner radius 0.02 pc (estimated from the ring size in Figure 3, bottom). The uncertainties in these tables do not include any uncertainty for choice of model, but an additional  $\sim 10\%$  should be added to the abundance uncertainties in the tables to account for the variations in the possible model parameters.

Notably, the oxygen abundance from the best-fitting model is super-solar (Table 6). With a low  $f$ , the fraction of elements in the highest ionization states (like  $\text{O}^{3+}$ ) is very small, and the oxygen abundance (O/H) becomes substantially higher than solar. We also searched for models of more compact PNe with lower  $f$  and smaller inner radii that produce a higher ionization fraction of oxygen. However, we found that none of these models could produce as strong [O IV] emission as is observed, unless the total oxygen abundance is substantially higher than Solar. In addition, because  $T_{\text{eff}}$  of the central star can be reliably determined from the He II 2.189  $\mu\text{m}$ /He I 2.059  $\mu\text{m}$  line ratio, and both  $\text{He}^{++}$  and  $\text{O}^{3+}$  require  $> 54$  eV photon energies for ionization to that level, the higher oxygen abundance is less affected

by the choice of the spectral energy distribution of the exciting star.

Along with oxygen, the helium abundance is also significantly higher than in SSTGC 588220. Because the emission from heavy element ions, especially oxygen, is the primary coolant for the gas, increasing their abundances results in lower electron temperatures, which in turn increases the emissivities of the hydrogen recombination lines much more than they change the emissivities of the He I 2.059  $\mu\text{m}$  line (see Storey & Hummer 1995; Porter et al. 2012, 2013). The consequence is that the abundance of helium with respect to hydrogen must be increased above Solar to match the observed line fluxes.

#### 4.3. [Kr III] 2.199 $\mu\text{m}$

In both candidate PNe, we detected the *s*-process noble gas krypton (Kr) at 2.199  $\mu\text{m}$ , which was first identified in PNe by Dinerstein (2001). From the line flux measurements, we computed the  $\text{Kr}^{++}/\text{H}^+$  ratios of  $(3.67 \pm 1.66) \times 10^{-9}$  and  $(1.36 \pm 0.13) \times 10^{-9}$  for SSTGC 580183 and SSTGC 588220, respectively, based on the Br  $\gamma$  emissivities of Storey & Hummer (1995), the effective collisional strengths for  $\text{Kr}^{++}$  of Schöning (1997), and the transition probabilities for  $\text{Kr}^{++}$  of Eser & Özdemir (2019). Because [Kr III] 2.199  $\mu\text{m}$  is not modeled in the current version of Cloudy, we adopted the analytical relation for the *ICF* from Sterling et al. (2015) between the  $\text{Kr}^{++}/\text{Kr}$  and the  $\text{S}^{++}/\text{S}$  ratios, which show the tightest fit among other ionic ratios (such as  $\text{Ar}^{++}/\text{Ar}$ ). In addition, our  $\text{S}^{++}/\text{S}$  ratio is more reliable than  $\text{Ar}^{++}/\text{Ar}$ , because the  $\text{S}^{++}$  and  $\text{S}^{3+}$  measurements were made using higher resolution modules in the IRS with less extinction. The Kr/H abundance ratios are included in Table 6.

#### 4.4. Significance

Krypton is significantly enriched in both of our targets ( $[\text{Kr}/\text{Fe}] = 1.4 \pm 0.3$  and  $0.4 \pm 0.2$  for SSTGC 580183 and SSTGC 588220, respectively)<sup>5</sup>, indicating that this *s*-process element has been over-produced, possibly during the late asymptotic giant branch evolution. This is in agreement with other lines of evidence supporting their status as a PN (morphology, high excitation lines, and a match to the PNe size-surface brightness relations) presented in this paper.

The abundance patterns of our targets are generally consistent with those in the GC region. Stars in this region have a bimodal metallicity distribution with peaks

at  $[\text{Fe}/\text{H}] \sim -0.5$  and  $\sim +0.3$ , and exhibit an elevated  $\alpha$ -element abundance in the metal-poor component, while the metal-rich counterpart shows near-solar abundance patterns (e.g., Schultheis et al. 2020). Our derived metallicities are  $[\text{Fe}/\text{H}] \approx -0.6$  for SSTGC 580183 and  $[\text{Fe}/\text{H}] \approx +0.1$  for SSTGC 588220, which coincide with each of the metallicity peaks. Our estimated  $\alpha$ -element abundances also seem to follow the observed abundance pattern – higher  $\alpha$ -element abundances of SSTGC 580183 ( $[\text{O}/\text{Fe}] = 1.2$ ,  $[\text{S}/\text{Fe}] = 1.0$ ), and lower abundances of SSTGC 588220 ( $[\text{O}/\text{Fe}] = 0.2$ ,  $[\text{Mg}/\text{Fe}] = 0.4$ ,  $[\text{S}/\text{Fe}] = 0.2$ ) – although the former estimates are significantly higher than the GC sample in Schultheis et al. (2020).

Our radial velocity measurements were based on nebular emission lines, instead of observations of a central star of a PN. Given that the expansion speed of a PN is an order of a few tens of  $\text{km s}^{-1}$ , our measurements are uncertain by this amount. A large positive radial velocity of SSTGC 580183 ( $v_r^{\text{LSR}} \sim +70 \text{ km s}^{-1}$ ) in the fourth Galactic quadrant and an extreme negative radial velocity of SSTGC 588220 ( $v_r^{\text{LSR}} = -150 \text{ km s}^{-1}$ ) in the first quadrant are at odds with the sense of rotation of the nuclear stellar disk (a positive correlation between  $v_r$  and  $l$ ), but there is a large scatter in the  $v_r$  vs.  $l$  diagram of stars in the nuclear bulge (Schönrich et al. 2015; Schultheis et al. 2020).

SSTGC 580183 is extremely helium-rich  $N(\text{He})/N(\text{H}) = 0.12$ , while SSTGC 588220 has a nearly solar helium abundance. According to the PN classification scheme in Peimbert (1978), the helium abundance of SSTGC 580183 is at the border between the helium- and nitrogen-rich PNe (Type I) and other types with normal helium abundances. Since Type I PNe are considered a descendant of a massive progenitor star ( $> 2 M_\odot$ ) by their super-helium and nitrogen abundances (see also Stanghellini & Haywood 2010), it is conceivable that the progenitor of SSTGC 580183 is also likely as massive as  $\sim 2 M_\odot$ . This implies that SSTGC 580183 originated from binary interactions of old stellar populations in the nuclear bulge, or from recent star formation in the CMZ.

## 5. DISCUSSION AND SUMMARY

In this paper, we have presented medium-resolution near-IR spectra taken with Gemini/GNIRS of two candidate PNe, which were serendipitously found in *Spitzer*/IRS spectra in close lines of sight to Sgr A\*. Besides showing strong emission lines in the mid-IR from several high-excitation ions, their appearance on high-resolution images is consistent with their being PNe. Moreover, our Gemini/GNIRS near-IR spectra reveal

<sup>5</sup> Here, we used a conventional notation,  $[\text{X}/\text{Y}] \equiv \log(N_{\text{X}}/N_{\text{Y}})_* - \log(N_{\text{X}}/N_{\text{Y}})_\odot$ , where  $\log N$  indicates abundances of specific elements.



strong emission from doubly ionized krypton in both targets, indicating over-production of *s*-process elements in the PN envelope. Their memberships in the nuclear stellar disk seem feasible from the proximity to the GC on the sky and distances based on a comparison to PN size-surface brightness relations, and are favored by our joint analysis of near- and mid-IR spectra, instead of belonging to other Galactic structural components. Our Cloudy modeling assumes uniform density and filling factors of these targets, but future observations with high spatial-resolution mapping in the various near- and mid-IR lines can potentially reveal high-density, or even high-excitation structures within the overall morphology of these sources.

The expected number of PNe in the nuclear bulge can be estimated from a comparison with other Galactic stellar components. The total stellar mass of the nuclear bulge ( $\sim 1.4 \times 10^9 M_{\odot}$ ; Launhardt et al. 2002) is approximately 10 times less massive than the classical bulge. If we assume that most stars in the nuclear bulge are as old as those in the bulge ( $\gtrsim 10$  Gyr), and simply scale the result obtained from the populations synthesis models in Moe & De Marco (2006) by stellar mass, there should be  $\sim 10^3$  PNe found in this region, although this estimate is uncertain by a factor of two or more. At the other extreme, if we scale the expected number from the stellar halo in Moe & De Marco (2006), the number of PNe decreases by a factor of  $\sim 10^2$  due to older ages of the system (a relatively shorter dissipation timescale of stellar envelopes), but this estimate is quite uncertain. On the observational ground, however, there are 8 PNe known in the Galactic globular clusters (Jacoby et al. 1997; Minniti et al. 2019), from which one can naively expect  $\sim 10^3$  PNe since the nuclear bulge is  $\sim 100$  times more massive than the entire globular cluster system in the Milky Way.

In this regard, the scarcity of known PNe in the nuclear bulge raises a more severe problem than the observed paucity of PNe in other Galactic components. This may be due to extreme foreground extinction towards the GC. Such an observational bias may exist, because the two PNe presented in this paper have the most compact sizes (implying early stages of PN evolution) as can be seen from the size-surface brightness distributions of other Galactic and extra-Galactic PNe (see Figures 8 and 9). Their compactness has even made them appear as ‘point-like’ sources in the original *Spitzer*/IRAC catalog (Ramírez et al. 2008). As a consequence, there could be more PNe in lines of sight toward the CMZ that are more difficult to detect due to extended envelopes with lower surface brightness in the high source-density, highly dust-obscured region.

On the other hand, if the observed lack of PNe is rooted in astrophysical origins, this may indicate that the PN formation channel such as binary interactions (e.g., Minniti et al. 2019) is overpowered by suppression mechanisms that can reduce the envelope mass of asymptotic giant branch (AGB) stars. Some stars can also skip the AGB phase and directly evolve into hot subdwarfs, if the envelope mass is not high enough. These AGB manqué stars can be formed from helium-rich progenitor stars by enhanced mass loss during the red giant branch evolution (Bressan et al. 2012).

While PNe are strikingly rare in the nuclear bulge, however, the number of the observed PNe is not greatly different from what one would expect from ongoing star formation in the CMZ, with a rate of  $\sim 0.1 M_{\odot} \text{ yr}^{-1}$  (e.g., An et al. 2011; Longmore et al. 2013). Since the PN lifetime is approximately  $\Delta t \sim 10^4$  years, the total mass of stars formed at any time interval  $\Delta t$  is  $\sim 10^3 M_{\odot}$ , if the star formation has proceeded constantly over the past few billion years. If stars as massive as  $2 M_{\odot}$  can evolve into a PN, for reasons described above, a total mass of PN progenitors would be  $\sim 20 M_{\odot}$  at any time. Therefore, the expected number of PNe would become  $\sim 5$ – $10$ , if the average progenitor mass is  $2$ – $4 M_{\odot}$  in the nuclear bulge. Indeed, Simpson (2018) find half a dozen more candidates with exceptionally high excited lines from neon and/or oxygen, in addition to the two sources included in this study, which serve as good PN candidates in this region. Future high-resolution narrow-band imaging or mid-IR spectroscopic surveys will help hunt for additional PNe in the nuclear bulge.

## ACKNOWLEDGMENTS

We thank Kris Sellgren and Harriet Dinerstein for many helpful and interesting discussions over the years. We thank Thomas Geballe for his technical assistance before and during the observing runs. J.H. and D.A. acknowledge support provided by the National Research Foundation of Korea (NRF) to the Center for Galaxy Evolution Research (2017R1A5A1070354) and by Basic Science Research Program through the NRF grant funded by the Ministry of Education (NRF-2018R1D1A1A02085433).

The Gemini data (Gemini program GS-2016A-Q-42, NOAO prop. ID 2016A-0431), acquired through the Gemini Observatory Archive at NSF’s NOIRLab and processed using the Gemini IRAF package, are based on observations obtained at the international Gemini Observatory, a program of NSF’s NOIRLab, which is managed by the Association of Universities for Research

in Astronomy (AURA) under a cooperative agreement with the National Science Foundation on behalf of the Gemini Observatory partnership: the National Science Foundation (United States), National Research Council (Canada), Agencia Nacional de Investigación y Desarrollo (Chile), Ministerio de Ciencia, Tecnología e Innovación (Argentina), Ministério da Ciência, Tecnologia, Inovações e Comunicações (Brazil), and Korea Astron-

omy and Space Science Institute (Republic of Korea). This work was enabled by observations made from the Gemini North telescope, located within the Maunakea Science Reserve and adjacent to the summit of Maunakea. We are grateful for the privilege of observing the Universe from a place that is unique in both its astronomical quality and its cultural significance.

## REFERENCES

- An, D., Ramírez, S. V., Sellgren, K., et al. 2009, *ApJL*, 702, L128. doi:10.1088/0004-637X/702/2/L128
- An, D., Ramírez, S. V., Sellgren, K., et al. 2011, *ApJ*, 736, 133. doi:10.1088/0004-637X/736/2/133
- An, D., Ramírez, S. V., & Sellgren, K. 2013, *ApJS*, 206, 20. doi:10.1088/0067-0049/206/2/20
- Asplund, M., Grevesse N., Sauval A. J., & Scott P. 2009, *ARA&A*, 47, 481. doi:10.1146/annurev.astro.46.060407.145222
- Balick, B. & Frank, A. 2002, *ARA&A*, 40, 439. doi:10.1146/annurev.astro.40.060401.093849
- Beaulieu S. F., Freeman K. C., Kalnajs A. J., Saha P., & Zhao H. 2000, *AJ*, 120, 855. doi:10.1086/301504
- Boogert, A. C. A., Huard, T. L., Cook, A. M., et al. 2011, *ApJ*, 729, 92. doi:10.1088/0004-637X/729/2/92
- Bressan, A., Marigo, P., Girardi, L., et al. 2012, *MNRAS*, 427, 127. doi:10.1111/j.1365-2966.2012.21948.x
- Chiar, J. E., & Tielens, A. G. G. M. 2006, *ApJ*, 637, 774. doi:10.1086/498406
- Cushing, M. C., Vacca, W. D., & Rayner, J. T. 2004, *PASP*, 116, 362. doi:10.1086/382907
- Dahmen, G., Huttemeister, S., Wilson, T. L., et al. 1998, *A&A*, 331, 959
- Dinerstein, H. L. 2001, *ApJ*, 550, L223. doi:10.1086/319645
- Durand, S., Acker, A., & Zijlstra, A. 1998, *ApJS*, 132, 13. doi:10.1051/aas:1998356
- Elias, J. H., Rodgers, B., Joyce, R. R., et al. 2006a, *Proc. SPIE*, 6269, 626914. doi:10.1117/12.671765
- Elias, J. H., Joyce, R. R., Liang, M., et al. 2006b, *Proc. SPIE*, 6269, 62694C. doi:10.1117/12.671817
- Eser, S., & Özdemir, L. 2019, *CJP*, 97, 529. doi:10.1139/cjp-2018-0385
- Fazio, G. G., et al. 2004, *ApJS*, 154, 10. doi:10.1086/422843
- Ferland, G. J., Chatzikos, M., Guzmán, F., et al. 2017, *RMxAA*, 53, 385
- Figer, D. F., McLean, I. S., & Morris, M. 1999, *ApJ*, 514, 202. doi:10.1086/306931
- Frew, D. J., Bojičić, I. S., & Parker, Q. A. 2016a, *Journal of Physics Conference Series*, 728, 032015. doi:10.1088/1742-6596/728/3/032015
- Frew, D. J., Parker, Q. A., & Bojičić, I. S. 2016b, *MNRAS*, 455, 1459. doi:10.1093/mnras/stv1516
- Fritz, T. K., Gillessen, S., Lutz, D., et al. 2011, *ApJ*, 737, 73. doi:10.1088/0004-637X/737/2/73
- Gaia Collaboration, Brown, A. G. A., Vallenari, A., et al. 2018, *A&A*, 616, A1. doi:10.1051/0004-6361/201833051
- Gravity Collaboration, Abuter, R., Amorim, A., et al. 2019, *A&A*, 625, L10. doi:10.1051/0004-6361/201935656
- Higdon, S. J. U., Devost, D., Higdon, J. L. et al. 2004, *PASP*, 116, 975. doi:10.1086/425083
- Houck, J. R., Roellig, T. L., van Cleve, J., et al. 2004, *ApJS*, 154, 18. doi:10.1086/423134
- Jacoby G. H., Kronberger, M., Patchick, D., et al. 2010, *PASA*, 27, 156. doi:10.1071/AS09025
- Jacoby, G. H., Morse, J. A., Fullton, L. K., et al. 1997, *AJ*, 114, 2611. doi:10.1086/118671
- Jacoby, G. H., & van de Steene, G. 2004, *A&A*, 419, 563. doi:10.1051/0004-6361:20035809
- Launhardt, R., Zylka, R., & Mezger, P. G. 2002, *A&A*, 384, 112. doi:10.1051/0004-6361:20020017
- Lawrence, A., Warren, S. J., Almaini, O., et al. 2007, *MNRAS*, 379, 1599. doi:10.1111/j.1365-2966.2007.12040.x
- Longmore, S. N., Bally, J., Testi, L., et al. 2013, *MNRAS*, 429, 987. doi:10.1093/mnras/sts376
- Manchado, A., Stanghellini, L., & Guerrero, M. A. 1996, *ApJL*, 466, L95. doi:10.1086/310170
- Mills, E., Morris, M. R., Lang, C. C., et al. 2011, *ApJ*, 735, 84. doi:10.1088/0004-637X/735/2/84
- Minniti, D., Dias, B., Gómez, M., et al. 2019, *ApJL*, 884, L15. doi:10.3847/2041-8213/ab4424
- Miszalski B., Parker Q. A., Acker A., Birkby J. L., Frew D. J., & Kovacevic A. 2008, *MNRAS*, 384, 525. doi:10.1111/j.1365-2966.2007.12727.x
- Moe, M., & De Marco, O. 2006, *ApJ*, 650, 916. doi:10.1086/506900

- Morris, M., & Serabyn, E. 1996, *ARA&A*, 34, 645.  
doi:10.1146/annurev.astro.34.1.645
- Nogueras-Lara, F., Schödel, R., Gallego-Calvente, A. T., et al. 2020, *Nature Astronomy*, 4, 377.  
doi:10.1038/s41550-019-0967-9
- Osterbrock, D. E. & Ferland, G. J. 2006, *Astrophysics of gaseous nebulae and active galactic nuclei*, 2nd. ed. by D.E. Osterbrock and G.J. Ferland. Sausalito, CA: University Science Books, 2006
- Parker, Q. A., Acker, A., Frew, D. J., et al. 2006, *MNRAS*, 373, 79. doi:10.1111/j.1365-2966.2006.10950.x
- Parker, Q. A., Cohen, M., Stupar, M., et al. 2012, *MNRAS*, 427, 3016. doi:10.1111/j.1365-2966.2012.21927.x
- Peimbert, M. 1978, *Planetary Nebulae*, 76, 215
- Peimbert, M., Peimbert, A., & Delgado-Inglada, G. 2017, *PASP*, 129, 082001. doi:10.1088/1538-3873/aa72c3
- Porter, R. L., Ferland, G. J., Storey, P. J., & Detisch, M. J. 2012, *MNRAS*, 425, L28.  
doi:10.1111/j.1745-3933.2012.01300.x
- Porter, R. L., Ferland, G. J., Storey, P. J., et al. 2013, *MNRAS*, 433, L89. doi:10.1093/mnras/slt049
- Ramírez, S. V., Arendt, R. G., Sellgren, K., et al. 2008, *ApJS*, 175, 147. doi:10.1086/524015
- Rauch, T. 2003, *A&A*, 403, 709.  
doi:10.1051/0004-6361:20030412
- Reid, M. J., Menten, K. M., Brunthaler, A., et al. 2019, *ApJ*, 885, 131. doi:10.3847/1538-4357/ab4a11
- Roche, P. F., & Aitken, D. K. 1985, *MNRAS*, 215, 425.  
doi:10.1093/mnras/215.3.425
- Sabin, L., Parker, Q. A., Corradi, R. L. M., et al. 2014, *MNRAS*, 443, 3388. doi:10.1093/mnras/stu1404
- Schöning, T. 1997, *AAS*, 122, 277. doi:10.1051/aas:1997133
- Schönrich, R., Aumer, M., & Sale, S. E. 2015, *ApJL*, 812, L21. doi:10.1088/2041-8205/812/2/L21
- Schultheis, M., Rojas-Arriagada, A., Cunha, K., et al. 2020, *A&A*, 642, A81. doi:10.1051/0004-6361/202038327
- Schultheis, M., Sellgren, K., Ramírez, S., et al. 2009, *A&A*, 495, 157. doi:10.1051/0004-6361:200810342
- Scott, P., Grevesse, N., Asplund, M., et al. 2015a, *A&A*, 573, A25. doi:10.1051/0004-6361/201424109
- Scott, P., Grevesse, N., Asplund, M., et al. 2015b, *A&A*, 573, A26. doi:10.1051/0004-6361/201424110
- Scoville, N. Z., Stolovy, S. R., Rieke, M., et al. 2003, *ApJ*, 594, 294. doi:10.1086/376790
- Serabyn, E. & Morris, M. 1996, *Nature*, 382, 602.  
doi:10.1038/382602a0
- Simpson, J. P. 2018, *ApJ*, 857, 59.  
doi:10.3847/1538-4357/aab55b
- Simpson, J. P., Colgan, S. W. J., Cotera, A. S., et al. 2007, *ApJ*, 670, 1115. doi:10.1086/522295
- Simpson, J. P. & Rubin, R. H. 1990, *ApJ*, 354, 165.  
doi:10.1086/168676
- Smith, J. D. T., Armus, L., Dale, D. A., et al. 2007, *PASP*, 119, 1113. doi:10.1086/522634
- Stanghellini, L., Bucciarelli, B., Lattanzi, M. G., et al. 2020, *ApJ*, 889, 21. doi:10.3847/1538-4357/ab59e4
- Stanghellini, L., & Haywood, M. 2010, *ApJ*, 714, 1096.  
doi:10.1088/0004-637X/714/2/1096
- Stanghellini, L., & Haywood, M. 2018, *ApJ*, 862, 45.  
doi:10.3847/1538-4357/aacaf8
- Sterling, N. C., Porter, R. L., & Dinerstein, H. L. 2015, *ApJS*, 218, 25. doi:10.1088/0067-0049/218/2/25
- Storey, P. J., & Hummer, D. G. 1995, *MNRAS*, 272, 41.  
doi:10.1093/mnras/272.1.41
- Tsuboi, M., Handa, T., & Ukita, N. 1999, *ApJS*, 120, 1.  
doi:10.1086/313165
- Wang, Q. D., Dong, H., Cotera, A., et al. 2010, *MNRAS*, 402, 895. doi:10.1111/j.1365-2966.2009.15973.x
- Werner, M. W., Roellig, T. L., Low, F. J., et al. 2004, *ApJS*, 154, 1. doi:10.1086/422992
- Yusef-Zadeh, F., Hewitt, J. W., & Cotton, W. 2004, *ApJS*, 155, 421. doi:10.1086/425257
- Zhang, Y., Liu, X.-W., Wesson, R., et al. 2004, *MNRAS*, 351, 935. doi:10.1111/j.1365-2966.2004.07838.x
- Zhao, J.-H., Morris, M. R., & Goss, W. M. 2020, *ApJ*, 905, 173. doi:10.3847/1538-4357/abc75e